Quantification of Mixing in a Numerical Model of an Estuary

Master Thesis

Fakultät für Informatik und Elektrotechnik

Universität Rostock

Nicky Prithvi Chandra Koganti, born on 30. December 1994 in Hyderabad, India

Supervisor and 1. Auditor : **Prof. Dr. Hans Burchard**,
Leibniz-Institute for Baltic Sea Research Warnemünde,
Universität Rostock

2. Auditor: **Marvin Lorenz M.Sc.**
Leibniz-Institute for Baltic Sea Research Warnemünde

Rostock, on 30. June 2020

Abstract

An estuary is a transition zone, where river water mixes with saline sea water. This process creates brackish water flowing into the ocean and saltwater entering the estuary. This estuarine exchange flow and the net mixing in an estuary can be associated with quantifying the salinity variance budget, where the mixing is defined as the rate of destruction of volume-integrated salinity variance. This mixing can be estimated by new relations that are derived using the well-known Knudsen relations and the Total exchange Flow (TEF) analysis framework. Also, the mixing is estimated for each salinity class or isohaline using the most recent universal law of estuarine mixing in isohaline coordinates. Further, the effective diahaline diffusivity is computed for each salinity class represented as a ratio of diahaline turbulent salinity transport and respective salinity gradient. These relations are tested here using the numerical model GETM (General Estuarine Transport Model) to simulate an idealized three-dimensional estuary under periodic flows (including monochromatic semi-diurnal tides and spring-neap cycle). Some of these relations are tested for the first time over the three-dimensional model and also under the forcing of spring-neap cycle. As a result, the mixing relations are tested and found that one of mixing relation deviates by 0% error and other by error of 28%. The mixing is also quantified in this numerical model using universal law of estuarine mixing over the entire estuary for every isohaline. Also, the effective diahaline diffusivity spatial distribution are plotted for a individual isohaline over the estuary.

Acknowledgements

I thank my supervisor Hans Burchard for providing me this opportunity to do my master thesis and teaching me how to approach a scientific problem. I also thank Marvin Lorenz for teaching and helping me with the tactics to handle GETM or coastal model in general and also patiently answering my stupid questions and doubts. Then, I would like to thank Xaver Lange for introducing me to GETM and also helping me with the post-processing. I thank Knut Klingbeil for around the clock support of GETM and solving the technical issues. Furthermore, I would like to thank all the people in physical oceanography and instrumentation department of IOW for helping to in completing my thesis and solving my programming problems. Last but not the least, I sincerely thank my parents and friends for supporting me throughout my education and career.

Contents

Chapter 1.

Introduction

An estuary is a coastal embayment, where a fresh river water meets the ocean. In estuaries, the salty ocean/sea mixes with fresh river water, resulting in brackish water. Brackish water is salty, but not as saline as ocean water. Estuary may also be called as bay, lagoon or slough.

The seawater which is higher in density than the river water tends to intrude beneath the river water outflow. Part of this intruded salted sea water mixes with river water and is returned to the sea by estuarine outflow in the upper water layer. This allows new seawater to enter estuary at the lower layer and creates a circulation of seawater. This is called estuarine circulation, which directs high saline water towards inland or riverside at the bottom and seaward at the surface. This estuarine circulation is driven by horizontal density gradient along the estuary. This mixing of salt water and river water is mainly due to turbulence generated by tides. The salt intrusions are the important phenomenon for the ecosystem, as they determine the limit of freshwater availability and the species living in an estuarine environment. This is where mixing determines the dispersion of salt and other dissolved substances along the estuary.

The inflow of seawater and outflow of the fresh river water is also known as the exchange flow. Initially, an early approach to estimate inflow and outflow volume transport and salinities was given by Knudsen (1900). As, the estuarine system is highly dominated by the density gradient mostly due to the salinity Walin (1977) proposed a theoretical framework based on continuous functions of salinity and time. Later, this framework was tested on Baltic sea (Walin, 1981). Combining these two concepts of Knudsen (1900) and Walin (1977), a new theory is proposed by MacCready and Geyer (2010) as Total Exchange Flow (TEF) analysis framework. The TEF framework is to calculate the time-averaged volume and mass transports in a closed volume of water

bodies (i.e oceans, estuaries, etc.). This TEF framework is also applied on the Baltic sea (Burchard et al., 2018).

The salinity mixing is quantified as a decay of ensemble averaged salinity variance as proposed by Burchard and Rennau (2008). Using this mixing quantification from salinity variance and TEF framework MacCready et al. (2018) has derived a bulk relation to estimation time-averaged and volume-integrated estuarine mixing. Later, Burchard et al. (2019) derived an exact Knudsen relation for mixing by using the concept of MacCready et al. (2018). These two mixing relations are derived for an estuary volume, bounded by a fixed transect. Further, extending this Burchard (2020) has presented a universal law of estuarine mixing, which dwells with mixing quantification in isohaline coordinates over the entire estuary rather than a fixed transect. Also, Burchard et al. (2020)(submitted) have developed a new idea of determining effective diahaline diffusivity from this universal law of estuarine mixing.

In this thesis, these methods of quantifying mixing are discussed and are applied to three-dimensional numerical model. The outline of my thesis is: presenting the governing equations applied in estuarine modeling, details on the mixing relations, a brief discussion on numerical model set-up and results from the numerical estuary model.

Chapter 2.

Theory

This chapter derives and discusses the basic governing equations, the hydrodynamic laws of Physical Oceanography used for this thesis such as Navier-Stokes equation, shallow water equations and Total Exchange Flow (TEF) analysis framework.

2.1. Governing equations

2.1.1. Navier-Stokes equations

The momentum equations describe the basic motion of particles which is derived from the Newton's Second law. In hydrodynamics the Navier-Stokes equation define the principles of fluid motion, the Navier-Stokes equation reads as:

$$\frac{\partial u_i}{\partial t} + \frac{\partial (u_i u_j)}{\partial x_j} + 2\epsilon_{ijk}\Omega_j u_k = -\frac{1}{\rho_0}\frac{\partial P}{\partial x_i} - \frac{g}{\rho_0}\rho\delta_{i3} + \nu\frac{\partial^2 u_i}{\partial x_j^2} \tag{2.1}$$

where u is velocity, ρ is density, g is acceleration due to gravity, P is pressure, ν is kinematic viscosity, Ω_j is Coriolis force (Earth rotation) and ρ_0 is the reference density (which is 1000 kg/m^3 for water).

The above Navier-Stokes equation (2.1) describes the change of momentum due to effect of forces (Coriolis force, pressure gradient, gravitational force, viscous force).

In equation (2.1), we assume that the density of fluid is constant, but not in the buoyancy term ($\frac{g}{\rho_0}\rho\delta_{i3}$). This is called Boussinesq assumption, which is widely used in fluid mechanics for ocean circulations.

As the result of Boussinesq assumption, the mass balance is similar to that of incompressible fluid, which is also referred as continuity equation

$$\frac{\partial u_i}{\partial x_i} = 0 \ . \tag{2.2}$$

2.1.2. Reynolds averaged Navier-Stokes equations

Most of the fluid flows occurring in nature are involving non predictable stochastic fluctuations which are called turbulent flows. This complicates to solve Navier-Stokes equation (2.1). To deal with this problem Reynolds decomposition is used. Where, a variable X is decomposed into mean part $\langle X \rangle$ (also known as ensemble average) and a fluctuating component X', such that $X = \langle X \rangle + X'$. Now, Reynolds decomposing the variables in Boussinesq approximated Navier-Stokes equation (2.1) and using ensemble averaging properties (see appendix A) result in the following Reynolds Averaged Navier-Stokes (RANS) equations:

$$\begin{aligned}\frac{\partial \langle u_i \rangle}{\partial t} + \frac{\partial (\langle u_i \rangle \langle u_j \rangle)}{\partial x_j} + 2\epsilon_{ijk}\Omega_j \langle u_k \rangle = -\frac{1}{\rho_0}\frac{\partial \langle P \rangle}{\partial x_i} - \frac{g}{\rho_0}\langle \rho \rangle \delta_{i3} \\ + \frac{\partial}{\partial x_j}\left(\nu \frac{\partial \langle u_i \rangle}{\partial x_j} - \langle u_i' u_j' \rangle\right) \ .\end{aligned} \tag{2.3}$$

Similarly, Reynolds Averaged continuity equation is

$$\frac{\partial \langle u_i \rangle}{\partial x_i} = 0 \ , \tag{2.4}$$

where $\langle u_i' u_j' \rangle$ is called as the Reynolds stress tensor. However, further attempt to solve these Reynolds stress tensor only leads to higher momentum terms like $\langle u_i' u_j' u_k' \rangle$ and so on. This is referred as the problem of turbulence closure.

2.1.3. Turbulence closure

In order to solve this turbulence closure problem, the Reynolds stress tensors are parameterized by introducing turbulent viscosity ν_t also known as eddy viscosity, which is first proposed by Boussinesq,

$$\langle u_i' u_j' \rangle = \frac{2}{3} k \delta_{ij} - \nu_t \left(\frac{\langle \partial u_i \rangle}{\partial x_j} + \frac{\langle \partial u_j \rangle}{\partial x_i} \right) . \tag{2.5}$$

Where k is turbulent kinetic energy, this equation (2.5) is also often called as Boussinesq hypothesis. Unlike the molecular viscosity which is constant with material, the turbulent viscosity is dependent on time and space. Depending on the Reynolds number of the flow, magnitude of the turbulent viscosity can be higher than material viscosity. In the present numerical setup $k - \epsilon$ turbulence closure is used (see 4.1), in which ν_t is computed as

$$\nu_t = c_\mu \frac{k^2}{\epsilon} , \tag{2.6}$$

where c_μ is the a non-dimensional adjustable constant and ϵ is the dissipation rate. These k and ϵ are calculated using equations which includes production and dissipation terms, for details see Umlauf and Burchard (2005).

2.1.4. Shallow water equations

The Reynolds Averaged Navier-Stokes equation (2.3) can be used to solve most of the fluid flow problems. These equations can be even simplified for the geophysical bodies like oceans, lakes, atmosphere etc. where the vertical scale H is smaller than the horizontal scale L. Doing a scale analysis for each term, by assuming $H/L \ll 1$ the following equations can be derived from equation (2.3) parameterized with turbulence closure, which are also called three-dimensional shallow water equations:

$$\frac{\partial\langle u\rangle}{\partial t}+\frac{\partial\langle u\rangle\langle u\rangle}{\partial x}+\frac{\partial\langle v\rangle\langle u\rangle}{\partial y}+\frac{\partial\langle w\rangle\langle u\rangle}{\partial z}-f\langle v\rangle=-\frac{1}{\rho_0}\frac{\partial\langle P\rangle}{\partial x}+\frac{\partial}{\partial z}\Big((\nu_t+\nu)\frac{\partial\langle u\rangle}{\partial z}\Big)\,, \tag{2.7}$$

$$\frac{\partial\langle v\rangle}{\partial t}+\frac{\partial\langle u\rangle\langle v\rangle}{\partial x}+\frac{\partial\langle v\rangle\langle v\rangle}{\partial y}+\frac{\partial\langle w\rangle\langle v\rangle}{\partial z}+f\langle u\rangle=-\frac{1}{\rho_0}\frac{\partial\langle P\rangle}{\partial y}+\frac{\partial}{\partial z}\Big((\nu_t+\nu)\frac{\partial\langle v\rangle}{\partial z}\Big)\,, \tag{2.8}$$

$$\frac{\partial\langle P\rangle}{\partial z}=-g\rho\,, \tag{2.9}$$

where f is Coriolis parameter defined as $f=2\Omega\sin\phi$, ϕ is latitude. The equation (2.9) is known as the hydrostatic equilibrium or hydrostatic balance equation. The pressure term P, is eliminated by vertical integrating hydrostatic equilibrium equation (2.9) from a position z to the water surface η. This results in following equation:

$$\frac{1}{\rho_0}\frac{\partial\langle P\rangle}{\partial x}=-g\frac{\partial\langle\eta\rangle}{\partial x}-\frac{g}{\rho_0}\int_z^\eta\frac{\partial\langle\rho\rangle}{\partial x}dz-\frac{1}{\rho_0}\frac{\partial\langle p_a\rangle}{\partial x}\,. \tag{2.10}$$

Hence, the horizontal pressure gradient includes all the contributions of sea surface slope (barotropic pressure gradient), density gradient (baroclinic pressure gradient) and the atmospheric pressure. Similar, it can be written for y-direction, shallow water equations (2.7) and (2.8) are deduced as below:

$$\frac{\partial\langle u\rangle}{\partial t}+\frac{\partial\langle u\rangle\langle u\rangle}{\partial x}+\frac{\partial\langle v\rangle\langle u\rangle}{\partial y}+\frac{\partial\langle w\rangle\langle u\rangle}{\partial z}-f\langle v\rangle=-g\frac{\partial\langle\eta\rangle}{\partial x}-\frac{g}{\rho_0}\int_z^\eta\frac{\partial\langle\rho\rangle}{\partial x}dz-\frac{1}{\rho_0}\frac{\partial\langle p_a\rangle}{\partial x}+\frac{\partial}{\partial z}\Big((\nu_t+\nu)\frac{\partial\langle u\rangle}{\partial z}\Big)\,, \tag{2.11}$$

$$\frac{\partial\langle v\rangle}{\partial t}+\frac{\partial\langle u\rangle\langle v\rangle}{\partial x}+\frac{\partial\langle v\rangle\langle v\rangle}{\partial y}+\frac{\partial\langle w\rangle\langle v\rangle}{\partial z}+f\langle u\rangle=-g\frac{\partial\langle\eta\rangle}{\partial y}-\frac{g}{\rho_0}\int_z^\eta\frac{\partial\langle\rho\rangle}{\partial y}dz \\ -\frac{1}{\rho_0}\frac{\partial\langle p_a\rangle}{\partial y}+\frac{\partial}{\partial z}\Big((\nu_t+\nu)\frac{\partial\langle v\rangle}{\partial z}\Big)\ . \tag{2.12}$$

Note that, the horizontal Reynolds stress tensors are neglected in the shallow water equations (2.11) and (2.12). These are only parameterized for the vertical components. As the high-resolution simulation used for the study sufficiently resolves the lateral and longitudinal dispersion. Hence, it is not necessary to parameterize it with horizontal diffusivity.

2.1.5. Boundary conditions

In general, there are two types of boundary conditions depending on the flow kinematics and material properties of the fluid. The Kinematic boundary conditions are derived from the arguments, that the fluid particles on the boundaries are at the same position independent of time. This condition has to be satisfied by the fluid irrespective of the material properties, and reads as:

$$w(\eta)=\frac{\partial\eta}{\partial t}+u(\eta)\frac{\partial\eta}{\partial x}+v(\eta)\frac{\partial\eta}{\partial y}\qquad\text{at free surface}\quad z=\eta(x,y,t)\ , \tag{2.13}$$

$$w(-H)=-u(-H)\frac{\partial H}{\partial x}-v(-H)\frac{\partial H}{\partial y}\qquad\text{at bottom}\quad z=-H(x,y)\ . \tag{2.14}$$

Now, by integrating the continuity equation (2.2) and using equations (2.13) and (2.14) the surface elevation η equation yields to:

$$\frac{\partial\eta}{\partial t}=-\frac{\partial}{\partial x}\int_H^\eta u(z)dz-\frac{\partial}{\partial y}\int_H^\eta v(z)dz \\ =-\frac{\partial U}{\partial x}-\frac{\partial V}{\partial y}\ , \tag{2.15}$$

where U and V are referred as horizontal transports. For the viscous fluids, so-called dynamic conditions can be derived under the assumption that the fluid particles adjacent to the solid boundaries moves with velocity of the wall (also known as no-slip condition), which reads as:

$$u = 0 \qquad \text{at bottom boundary} \quad z = -H(x, y) \ , \tag{2.16}$$

where it equivalent to Dirichlet-type boundary conditions. A von Neumann boundary condition can also be expressed using momentum flux instead of momentum itself, which reads as:

$$\nu \frac{\partial u}{\partial n} = \frac{\tau^b}{\rho_0} \qquad \text{at bottom} \quad z = -H(x, y) \ , \tag{2.17}$$

$$\nu \frac{\partial u}{\partial n} = \frac{\tau^s}{\rho_0} \qquad \text{at free surface} \quad z = \eta(x, y, t) \ , \tag{2.18}$$

where τ^b and τ^s are the momentum fluxes into the fluid at bottom and surface respectively and n denotes the normal outward vector on the boundaries.

2.1.6. Tracer equations

Density ρ of seawater is given by temperature and salt content of the water. Where, density ρ is a parameter in the Navier-Stokes equation (2.1) and in the shallow water equations (2.11),(2.12). Hence, the temperature θ and salinity S are also important for the dynamics as density is influenced by these parameters. Presently, we assume density ρ is only influenced by salinity S as temperature factors are not considered in the current study. Thus, density is computed from Gibbs function formulation based on thermodynamic properties of seawater (TEOS-10, `www.teos-10.org`, McDougall and Barker, 2011). Which is being used as standard for computing density since 2010.

The salinity equation with no source or sink as input can be written as:

$$\frac{\partial\langle s\rangle}{\partial t}+\frac{\partial\langle u\rangle\langle s\rangle}{\partial x}+\frac{\partial\langle v\rangle\langle s\rangle}{\partial y}+\frac{\partial\langle w\rangle\langle s\rangle}{\partial z}-\frac{\partial}{\partial z}\Big((\nu_t'+\nu^s)\frac{\partial\langle s\rangle}{\partial z}\Big)=0\ , \tag{2.19}$$

where ν^s is molecular diffusivity of salt and ν_t' is eddy diffusivity of salt. The eddy diffusivity is the parameter to close the eddy fluxes $\langle u's'\rangle$, or can also be stated as a parameter determined for the diffusion of salt caused by the turbulence in the fluid.

There are zero salinity fluxes added from the surface and zero fluxes from the bottom. Hence, the boundary conditions can be given as:

$$(\nu_t'+\nu^s)\frac{\partial\langle s\rangle}{\partial z}\bigg|_{z=\nu}=0 \qquad \text{and} \qquad (\nu_t'+\nu^s)\frac{\partial\langle s\rangle}{\partial z}\bigg|_{z=-H}=0 \tag{2.20}$$

Therefore, no evaporation or precipitation and no salt intrusion from the bottom bed are considered in this study.

2.2. Estuarine circulation

Estuaries are a complex system with nonlinear coupling of circulation and density structure. The first classical estuarine circulation theory was developed by Hansen and Rattray (1965), later many other authors have refined the theory to understand better physics of the estuarine circulation.

2.2.1. Dynamics of estuarine circulation

To study the classical dynamics of estuarine circulation, a one-dimensional problem is considered. In most of the simple quantitative model of estuarine circulation, Earth rotation, horizontal velocity gradients and atmospheric pressure gradient are neglected from the shallow water equation (2.11). This leads to the following:

$$\frac{\partial\langle u\rangle}{\partial t}-\frac{\partial}{\partial z}\Big((\nu_t+\nu)\frac{\partial\langle u\rangle}{\partial z}\Big)=-g\frac{\partial\langle\eta\rangle}{\partial x}-\frac{g}{\rho_0}\int_z^0\frac{\partial\rho}{\partial x}dz\ . \tag{2.21}$$

The above equation can be further simplified by assuming a spatially constant horizontal density gradient as follows:

$$\frac{\partial\langle u\rangle}{\partial t} - \frac{\partial}{\partial z}\Big((\nu_t+\nu)\frac{\partial\langle u\rangle}{\partial z}\Big) = -g\frac{\partial\langle\eta\rangle}{\partial x} - zb_x \ , \tag{2.22}$$

with

$$b_x = \frac{\partial b}{\partial x} = -\frac{g}{\rho_0}\frac{\partial\rho}{\partial x} \ . \tag{2.23}$$

Considering the temporal average of periodically oscillating solution $\bar{u}$ and neglecting the molecular viscosity, the equation is as follows:

$$-\frac{\partial}{\partial z}\Big(\nu_t\frac{\partial\bar{u}}{\partial z}\Big) = -g\bar{\eta}_x - zb_x \ , \tag{2.24}$$

where $\bar{\eta_x}$ is the temporally averaged surface elevation gradient.

An analytical solution for the estuarine circulation equation (2.24) is given by Hansen and Rattray (1965), (see also MacCready and Geyer (2010)) considering constant eddy viscosity ν_t and assuming no wind stress is given as below:

$$\bar{u}(z) = \frac{b_x H^3}{48\nu_t}\left[8\left(\frac{z}{H}\right)^3 + 9\left(\frac{z}{H}\right)^2 - 1\right] - \frac{3}{2}\left[\left(\frac{z}{H}\right)^2 - 1\right]u_r \ , \tag{2.25}$$

with

$$u_r = \frac{1}{H}\int_{-H}^{0} u(z)dz \ , \tag{2.26}$$

where u_r is the vertically and tidally averaged residual run-off velocity and H is the water depth. The analytical solution (2.25) strongly depends on u_r and on the factor $\frac{b_x H^3}{48\nu_t}$ which is also known as exchange flow intensity.

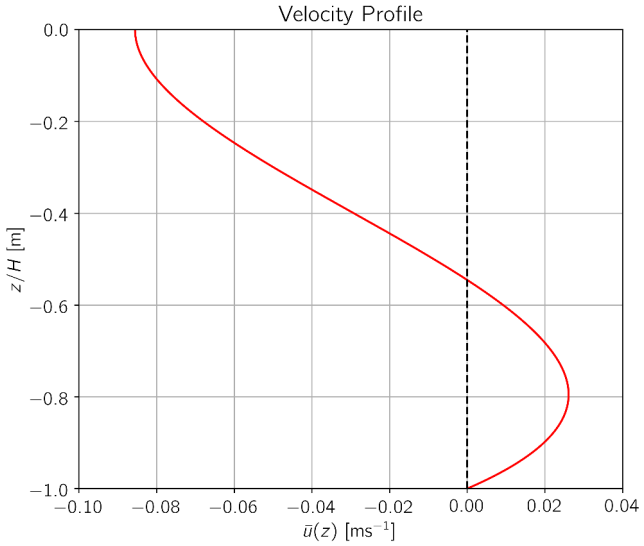

Figure 2.1.: Velocity profile $\bar{u}(z)$ for the analytical solution (2.25) with $H = 20$ m, $b_x = 10^{-6}$ s^{-2}, $\nu_t = 3 \cdot 10^{-3}$ m^{2}s^{-1} and $u_r = -0.02$ ms^{-1}.

The Fig 2.1 shows the classical estuarine circulation with an outflow at the surface and an inflow at the bottom.

2.2.2. Knudsen relations

The basic dynamics of estuarine circulation described in the previous section can be used to determine the exchange flows in estuaries. The estimation of exchange flow in the estuaries was first described by Knudsen (1900) using a bulk formulas, which are later known as Knudsen relations.

This is done by evaluating volume and salinity balance in a two-layered closed system. The out-flowing upper layer salinity is considered as s_{out} and the bottom layer in-flowing salinity as s_{in}. And assuming a steady state or periodic variability in time the following budgets can be evaluated:

1. The volume balance is as:

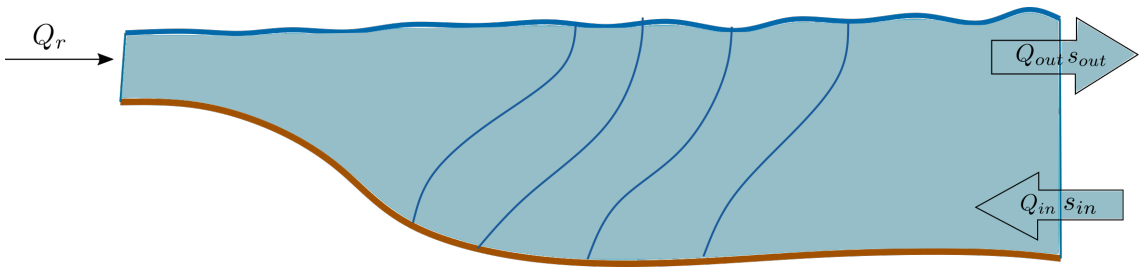

Figure 2.2.: Visualization of volume fluxes in an estuary: On left shows the river fluxes with zero salinity flowing into the estuary. On right is the ocean boundary, shows the exchange flow with the ocean. The blue lines indicate the isohalines with constant salinity.

$$Q_{in} + Q_{out} + Q_r = 0 \ , \tag{2.27}$$

where Q_{in} is inflow volume transport, Q_{out} is outflow volume transport and Q_r is river volume transport.

2. The salinity balance is as:

$$Q_{in}s_{in} + Q_{out}s_{out} = 0 \ . \tag{2.28}$$

The following Knudsen (1900) relations can be derived combining the above equations (2.27) and (2.28) as:

$$Q_{in} = \frac{s_{out}}{s_{in} - s_{out}} Q_r, \quad Q_{out} = \frac{-s_{in}}{s_{in} - s_{out}} Q_r \ . \tag{2.29}$$

From the relations one can say that the inflow and outflow volume fluxes can be calculated just with the information of inwards and outwards flowing currents salinities and river run-off.

2.2.3. Total Exchange Flow

The term "Total Exchange Flow" (TEF) was described by MacCready (2011) where the estuarine salinity and volume fluxes are investigated in the isohaline coordinates instead of the spatial coordinates.

For any tracer c, the outward total(advective plus diffusive) flux at a boundary can be defined as:

$$F^c = u_n c - K_h \partial_n c \ , \tag{2.30}$$

where F^c is the flux of tracer c, u_n is the normal velocity component. Now, the tidally averaged transports of the tracer c over the cross-section $A(S)$ can be expressed as:

$$Q^c(S) = -\left\langle \int_{A(S)} F^c dA \right\rangle \text{ and } q^c(S) = \frac{\partial Q^c(S)}{\partial S} \ , \tag{2.31}$$

where $A(S)$ is the tidally varying portion of cross-section with salinity s greater than S, $Q^c(S)$ is the incoming transport of c flowing through the cross-sectional area $A(S)$ with salinities s higher than S, and $q^c(S)$ is the incoming boundary flux of c per salinity class.

The inflow and outflow bulk values of any tracer c are defined as:

$$Q^c_{in} = \int_0^{S_{max}} (q^c)^+ dS \geq 0, \ \ Q^c_{out} = \int_0^{S_{max}} (q^c)^- dS \leq 0 \ , \tag{2.32}$$

where $(q^c)^+$ indicates positive part of the function (q^c), $(q^c)^-$ indicates negative part of the function (q^c) which give positive inflow transports and negative outflow transports, the volume fluxes can be calculated with $c = 1$ as:

$$Q(S) = -\left\langle \int_{A(S)} F dA \right\rangle \text{ and } q(S) = \frac{\partial Q(S)}{\partial S} \ . \tag{2.33}$$

Similarly, the inflow and outflow bulk values are:

$$Q_{in} = \int_0^{S_{max}} (q)^+ dS \geq 0, \;\; Q_{out} = \int_0^{S_{max}} (q)^- dS \leq 0 \; . \tag{2.34}$$

From the equations (2.32) and (2.34) the tracer concentrations flowing into and flowing out of the estuary can be calculated as:

$$c_{in} = \frac{Q^c_{in}}{Q_{in}}, \qquad c_{out} = \frac{Q^c_{out}}{Q_{out}} \; . \tag{2.35}$$

In above stated relations the tracer c can be any tracer (Walin, 1977). Presently, in the following study we use c=s, s^2 and s'^2 for salinity, salinity-squared and salinity variance respectively.

Chapter 3.

Mixing in estuaries

In general, mixing is associated with eddy viscosity or diffusivity. However, this cannot be used as a suitable means to measure mixing. For example, in a well mixed estuary the salinity mixing vanishes despite the high value of eddy diffusivity. To solve this issue, Burchard and Rennau (2008) had suggested a way to quantify mixing from conservation of salinity variance. Further, MacCready et al. (2018) and Burchard et al. (2019) had developed the following mixing relation using the concept of salinity variance.

3.1. Exact mixing relations

Now, the following mixing relation are derived for time dependent estuaries cases considering mass and salinity conservation as shown in Burchard et al. (2019).

From the volume integrating the continuity equation (2.4), volume budget in the estuary is expressed as

$$\partial_t V = -\int_{A(0)} u_n dA - \int_{A_r} u_n dA \tag{3.1}$$

where $A(0)$ is the open boundary transect area for salinities larger than zero, typically located at open boundary and A_r is the area through which freshwater of zero salinity is discharged into the control volume. u_n is the normal velocity component (positive outwards estuary).

Similarly, volume integrating the salinity equation (2.19) results in,

$$\partial_t \int_V s dV = -\int_{A(0)} F^s dA \ , \tag{3.2}$$

where F^s is referred as effective salinity flux

$$F^s = u_n s - K_v \partial_z s \ . \tag{3.3}$$

Now, if we multiply the salinity equation (2.19) with $2s$, we obtain a salinity squared equation

$$\partial_t s^2 + \partial_x (u s^2) + \partial_y (v s^2) + \partial_z (w s^2) - \partial_z (K_v \partial_z s^2) = -\chi^s \ , \tag{3.4}$$

where χ^s is the local salt mixing, see Burchard and Rennau (2008),

$$\chi^s = 2[K_h (\partial_x s)^2 + K_h (\partial_y s)^2 + K_v (\partial_z s)^2] \ . \tag{3.5}$$

Integrating the s^2 equation (3.4) over the total volume V results in

$$\partial_t \int_V s^2 dV = -\int_{A(0)} F^{s^2} dA - M \ , \tag{3.6}$$

with

$$F^{s^2} = u_n s^2 - K_v \partial_z s^2 \ , \tag{3.7}$$

where F^{s^2} is the effective salinity squared flux at the open boundary and M is the volume-integrated mixing

$$M = \int_V \chi^s dV \ . \tag{3.8}$$

Using the equation (3.4), rewriting salinity as $s = \bar{s} + s'$ and multiplying $2\bar{s}$ to salinity equation (2.19), salinity variance squared equation is derived (see appendix B) as:

$$\partial_t s'^2 + \partial_x(us'^2) + \partial_y(vs'^2) + \partial_z(ws'^2) - \partial_z(K_v \partial_z s'^2) = -\chi^s - 2s'\partial_t \bar{s} \ . \tag{3.9}$$

Volume integrating the salinity variance squared equation (3.9), results in the following salinity variance budget:

$$\partial_t \int_V s'^2 dV = -\int_{A(0)} F^{s'^2} dA - \overline{s}^2 \int_{A_r} u_n dA - M \ , \tag{3.10}$$

with

$$F^{s'^2} = u_n s'^2 - K_v \partial_z s'^2 \ , \tag{3.11}$$

where $s' = s - \overline{s}$ is the salinity deviation and $\overline{s} = (1/V) \int_V s dV$ is the volume-averaged salinity. For further details see equation (2) and (3) of MacCready et al. (2018). Now, comparing the (3.6) equation and variance equation (3.10), there is additional term of freshwater input (on the right-hand side). The salinity variance budget is more clearly related to the concept of molecular mixing, and it highlights the importance of river flow as a source of unmixed high-variance water. We define the temporal averaged fresh-water as,

$$Q_r = -\left\langle \int_{A_r} u_n dA \right\rangle . \tag{3.12}$$

Now, using transport fluxes equation (2.31) from TEF framework, the volume integral budget equation (3.1) is transformed as

$$V_{stor} = \langle \partial_t V \rangle = \int_0^{S_{max}} q(S) dS + Q_r = Q_{in} + Q_{out} + Q_r \ , \tag{3.13}$$

the salinity integral budget (3.2) as

$$S_{stor} = \langle \partial_t (\bar{s} V) \rangle = \left\langle \partial_t \int_V s dV \right\rangle = \int_0^{S_{max}} q^s(S) dS = Q_{in} s_{in} + Q_{out} s_{out} \ , \tag{3.14}$$

volume integrated salinity squared budget (3.6) as

$$\begin{aligned} (S^2)_{stor} = \langle \partial_t (\bar{s^2} V) \rangle = \left\langle \partial_t \int_V s^2 dV \right\rangle &= \int_0^{S_{max}} q^{s^2}(S) dS - \langle M \rangle \\ &= Q_{in} (s^2)_{in} + Q_{out} (s^2)_{out} - \langle M \rangle \ , \end{aligned} \tag{3.15}$$

and salinity variance squared volume integrated budget (3.10) as

$$\begin{aligned} (S'^2)_{stor} &= \langle \partial_t (\bar{s'^2} V) \rangle = \left\langle \partial_t \int_V s'^2 dV \right\rangle \\ &= \int_0^{S_{max}} q^{s'^2}(S) dS - \left\langle \bar{s}^2 \int_{A_r} u_n dA \right\rangle - \langle M \rangle \\ &= Q_{in} (s'^2)_{in} + Q_{out} (s'^2)_{out} - \left\langle \bar{s}^2 \int_{A_r} u_n dA \right\rangle - \langle M \rangle \ . \end{aligned} \tag{3.16}$$

Where $\bar{s^2}$ is volume averaged salinity squared and $\bar{s'^2}$ is volume-averaged salinity variance. V_{stor}, S_{stor}, $(S^2)_{stor}$ and $(S'^2)_{stor}$ are the storage terms for volume, salinity, salinity-squared, and salinity variance respectively. In periodic case, when properly averaged over one or more periodic tides these storage terms are equal to zero.

$$
\begin{aligned}
Q_{in} &= \frac{s_{out}}{s_{in} - s_{out}} Q_r - \frac{s_{out}}{s_{in} - s_{out}} V_{stor} + \frac{1}{s_{in} - s_{out}} S_{stor} \ , \\
Q_{out} &= -\frac{s_{in}}{s_{in} - s_{out}} Q_r + \frac{s_{in}}{s_{in} - s_{out}} V_{stor} - \frac{1}{s_{in} - s_{out}} S_{stor} \ ,
\end{aligned}
\tag{3.17}
$$

the time-independent Knudsen relation (2.29) can be obtained by assuming V_{stor} = S_{stor} = 0.

From these equations (3.17) and with salinity squared stored term (3.15), we can derive four different Knudsen relations for mixing, depending on the assumption of periodicity and constancy (Burchard et al., 2019).

1. For non-constancy[$(s^2)_{in} \neq (s_{in})^2$ and $(s^2)_{out} \neq (s_{out})^2$] and non-periodicity, we obtain exact mixing relation,

$$
M_e = \frac{s_{out}(s^2)_{in} - s_{in}(s^2)_{out}}{s_{in} - s_{out}} (Q_r - V_{stor}) + \frac{(s^2)_{in} - (s^2)_{out}}{s_{in} - s_{out}} S_{stor} - (S^2)_{stor} \ . \tag{3.18}
$$

2. Now, assuming both periodicity and constancy [$(s^2)_{in} = (s_{in})^2$ and $(s^2)_{out} = (s_{out})^2$], the simplified mixing relation is,

$$
M_{cp} = s_{in} s_{out} Q_r \ . \tag{3.19}
$$

The latter equation (3.19) is also derived with time-independent Knudsen-relation as shown in MacCready et al. (2018) and also see section 2 in Burchard et al. (2019).

3.2. Universal law of estuarine mixing

In the previous mixing relations (3.8), the mixing is estimated when the estuary is separated from ocean by a transect T which is fixed in time. Hence, in the equation (3.19) the salinities s_{in} and s_{out} are inflow and outflow salinities flowing through the transect T. These salinities are calculated using the Knudsen (1900) relations and Q_r is the average freshwater runoff into the estuary volume bounded by transect T.

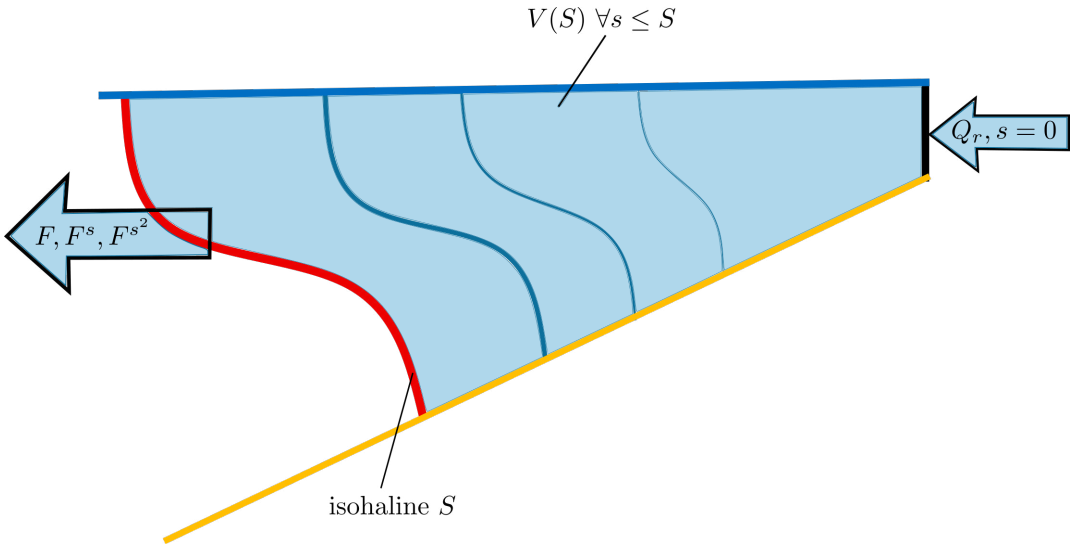

Figure 3.1.: Sketch for transport fluxes with respect to the isohaline S, modified after Burchard (2020).

In general, classical estuaries are dominated by salinity gradient. Hence, Burchard (2020) has described a different approach by considering a certain isohaline S as the boundary for estuary instead of transect T. This kind of framework using salinity as a coordinate to analyze the estuarine systems was proposed by Walin (1977). The mixing in estuary volume bounded by an isohaline S is given as,

$$M = \left\langle \int_{V(S)} \chi^s dV \right\rangle , \tag{3.20}$$

where the volume of estuary $V(S)$ includes all the salinities $s \leq S$. Assuming conditions of periodicity for long-term averaging, the averaged volume transport through the isohaline S equals the freshwater flux Q_r and it does not depend on S, assuming all river runoff occur at zero salinity. The inflow and outflow salinities occurring at the bounded isohaline S would be $s_{in} = s_{out} = S$. All the salinity fluxes are bounded by the isohaline S. The simplified mixing relation will be,

$$M(S) = S^2 Q_r \ . \tag{3.21}$$

Now, using salinity as a vector space, i.e in salinity classes ranging from 0 to S the mixing per salinity class is

$$m(S) = \partial_S M(S) = 2SQ_r \ , \tag{3.22}$$

where $m(S)$ is the mixing within an infinitesimal salinity interval δS centered around the isohaline S. Integrating $m(S)$ from 0 to S gives $M(S)$.

Equation (3.22) implies a fundamental law of estuarine physics: the long-term averaged mixing per salinity class in any estuary is twice the product of the salinity and the freshwater runoff (Burchard, 2020).

3.3. Effective diahaline diffusivities in estuary

As previously stated mixing is associated with eddy viscosity or diffusivity. According to Hansen and Rattray (1965) the intensity of estuarine exchange flow is inversely proportional to the specified constant vertical eddy viscosity and diffusivity. Also, from the numerical model study of Hetland and Geyer (2004) showed that eddy viscosity and diffusivity impacts the longitudinal extent of the brackish water zone (i.e estuary length), higher eddy coefficient result in shorter estuary and vice-verse.

As eddy diffusivity plays an important role in estuarine circulation, there is a recently presented study on estimating the diahaline turbulent salinity fluxes and diffusivities in an numerical model by Burchard et al. (2020, submitted), which are calculated using the previously presented mixing relations.

As previously presented χ^s as local loss of salinity variance (Burchard and Rennau, 2008), is represented as:

$$\chi^s = 2[K_h(\partial_x s)^2 + K_h(\partial_y s)^2 + K_v(\partial_z s)^2] = -2\vec{\mathscr{F}}^s_{\rm diff} \cdot \vec{\nabla} s \ . \tag{3.23}$$

To be noted that, single components of the turbulent salinity flux vector are down-gradient, but due to the non-isotropic eddy diffusivity ($K_h \gg K_v$) the entire vector

itself is generally not down-gradient. Hence, it is not orthogonal to the isohaline surface (Burchard et al., 2020, submitted).

So, for isohaline surface the total (advective plus diffusive) diahaline salinity flux is defined as

$$F^s = F^s_{\mathrm{adv}} + F^s_{\mathrm{diff}} = u_n s - K_n \partial_n s \ , \tag{3.24}$$

where u_n is the outgoing velocity normal to $\vec{n} = \vec{\nabla} s / |\vec{\nabla} s|$ (pointing towards higher salinity), $\partial_n s$ is the salinity gradient and K_n denotes diahaline diffusivity. Note that, the diahaline turbulent salinity flux $F^s_{\mathrm{diff}} = \vec{\mathscr{F}}^s_{\mathrm{diff}} \cdot \vec{n}$, is the orthogonal projection of turbulent salinity flux vector to the isohaline surface.

Using equation (3.23), diahaline turbulent salinity flux (3.24) and considering only diffusion terms, K_n diahaline diffusivity can be expressed as:

$$K_n = -\frac{F^s_{\mathrm{diff}}}{\partial_n s} = \frac{K_h (\partial_x s)^2 + K_h (\partial_y s)^2 + K_v (\partial_z s)^2}{(\partial_n s)^2} = \frac{\frac{1}{2}\chi^s}{(\partial_n s)^2} \ . \tag{3.25}$$

According to Walin (1977) the isohaline volume is defined as the infinitesimal volume per salinity class, which can be formulated as:

$$v(S) = \partial_S V(S) = \partial_S \int_0^S v(S') dS' = \left\langle \int_{A(S)} (\partial_n s)^{-1} dA \right\rangle \ . \tag{3.26}$$

Using equations (3.25) and (3.26), mixing per salinity class can also be expressed as

$$
\begin{aligned}
m &= \left\langle \int_{A(S)} (\partial_n s)^{-1} \chi^s dA \right\rangle \\
&= \left\langle \int_{A(S)} (\partial_n s)^{-1} 2K_n (\partial_n s)^2 dA \right\rangle \\
&= \left\langle \int_{A(S)} K_n \partial_n s dA \right\rangle \\
&= -2F^s_{\text{diff}} \ ,
\end{aligned}
\tag{3.27}
$$

where $-2F^s_{\text{diff}}$ is the diahaline turbulent salinity transport. Motivated by the equation (3.25), the effective total diahaline diffusivity $\overline{K_n}$ can be calculated by dividing the negative mean diahaline turbulent flux averaged over the isohaline surface $-F^s_{\text{diff}}/a$ with the mean diahaline salinity gradient $b^{-1} = a/v$. Where, a is the isohaline area, v is the volume per salinity class and b can also be referred as the isohaline thickness. Also, this can be further simplified by using relation (3.27) and substituting $-F^s_{\text{diff}}$ in terms of m as:

$$
\overline{K_n} = \frac{-F^s_{\text{diff}}/a}{b^{-1}} = \frac{1}{2}\frac{mv}{a^2} \ . \tag{3.28}
$$

So, using this equation the effective diahaline diffusivity can be estimated for an isohaline without any need to salinity squared budget estimation. Also, $\overline{K_n}$ is dependent on salinity gradient b^{-1}. From this, one can argue that the diahaline diffusivities are different for each tracer although the horizontal and vertical diffusivities are not.

Chapter 4.

Idealized estuary simulation

4.1. Model setup

To quantify the mixing and analyze the mixing relation derived in the previous chapter (3), an idealized estuary is simulated. This model estuary is located at $53.5°$N latitude stretched across a length of 100 km. The estuarine channel has a minimum width of 1 km at riverside and exponentially increasing mouth opening at the ocean boundary of width 81 km. And the central navigational channel is of 15 m depth, with an average lateral shoals depth of 3 m (see Fig 4.1).

For the simulations, the General Estuarine Transport Model (GETM, `www.getm.eu`, Burchard and Bolding, 2002; Gräwe et al., 2015) has been applied, a primitive equation coastal ocean model using general vertical coordinates and explicit mode splitting. It is coupled to the turbulence module of the General Ocean Turbulence Model (GOTM, `www.gotm.net`, Burchard and Bolding, 2001; Umlauf and Burchard, 2005), using the k-ε two-equation turbulence closure model with an algebraic second-moment closure by Cheng et al. (2002). Explicit horizontal diffusion is not applied.

A curvi-linear grid is constructed with 200 cells in longitudinal direction and 30 cells across the estuary. In the vertical, 30 σ-layers are used with some grid refinement towards the bottom. For the temporal discretization, each tidal cycle is resolved with 5000 baroclinic and 50000 barotropic equidistant time steps. The advection terms in the momentum, salinity and turbulence budgets are discretized by means of TVD-SPL-max-1/3 scheme (Waterson and Deconinck, 2007) using Strang splitting (Pietrzak, 1998).

This model is simulated from rest with zero elevation, zero velocity and with constant salinity of 15 g/kg to a quasi-steady state. The open boundary at the ocean has a salinity of 35 g/kg. A constant freshwater (i.e zero salinity) river-runoff of Q_r =700 m^3s^{-1} is prescribed at river boundary. Two different tidal forcings are investigated in the following:

(i) Monochromatic semi-diurnal tide amplitude of 2 m

(ii) Spring-Neap tidal cycle with amplitudes of 2.5 m (spring tide) and 1.5 m (neap tide). Which is the resultant of lunar semi-diurnal(M_2) tide with amplitude of 2 m and solar semi-diurnal (S_2) tide of 0.5 m.

4.2. Results and discussion

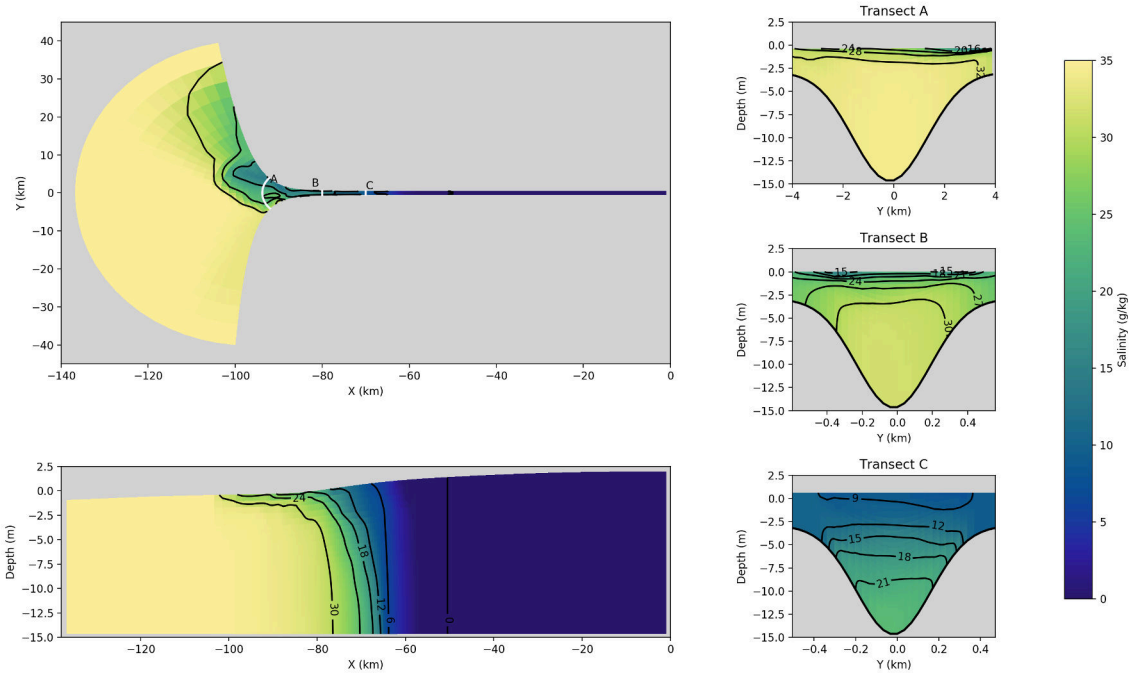

Figure 4.1.: Salinity distributions of the estuary forced with monochromatic semi-diurnal tide. The upper left figure shows surface salinity, lower left figure show longitudinal transect at y=0 km, and the figures on right shows the cross-sectional transects at three different location (x= -90 km, -80 km, and -70 km). The black lines indicate the salinity isohalines.

The idealized model is run until a quasi-periodic state is reached. The last 10 tidal periods are taken to examine the presented mixing relations in the previous chapters. The Fig 4.1 is a snapshot of the simulation, taken where the salt-wedge is located furthest into estuary with a strong stratification downstream. It is also visible that the river plume at the mouth of estuary is steering towards the North (i.e towards positive y-direction) due to Earth rotation.

For calculating the bulk quantities with the TEF framework, the methods of Lorenz et al. (2019) was used with 0.1 salinity bin width (δS). Since, it solves the numerical issues of TEF framework for realistic exchange flows (i.e two or more layer exchange flows). Also, the mixing value from the relations are compared with the mixing value of numerical model. In general, for a numerical model the mixing is combination of both numerical and physical, this numerical mixing is contributed by discretization of tracer quantities for the advective terms (Burchard and Rennau, 2008). In the following study the mixing is decomposed into physical and numerical mixing, using the method of Klingbeil et al. (2014).

4.2.1. Results of monochromatic semi-diurnal tides

The exchange flow profiles Fig 4.2 are investigated at transect B. From the profiles, inflow occurs around the range of $S > 26$ g/kg and outflow over the salinity range less than 26 g/kg. The highest transports (volume, salinity and salinity-squared) flowing into the estuary occurs around ≈ 31 g/kg salinity. Also, the river-runoff can be estimated from the volume transport at zero salinity i.e $Q(0) = 700$ m^{3}s^{-1}. From the volume transport profiles, it can be said that this is a two-layered classical exchange flow.

Table 4.1 shows the details of inflow and outflow transports of estuary at transect B (i.e, x= -80 km). The mean salinity range at which the inflow occurs is ≈ 31 g/kg, and the outflow water salinity is ≈ 12 g/kg. The storage terms $\langle V_{stor} \rangle$, $\langle S_{stor} \rangle$ and $\langle (S^2)_{stor} \rangle$ are not equal to zero. This implies that, estuary is not completely periodic as there is a change in transport budgets of estuary over time.

The mixing diagnosed from the numerical simulation $\langle M \rangle$ exactly equals the mixing computed from the exact mixing relation $\langle M_e \rangle$. Whereas, the mixing relation $\langle M_{cp} \rangle$ assuming time-independence (i.e $\langle V_{stor} \rangle = \langle S_{stor} \rangle = \langle (S^2)_{stor} \rangle = 0$) and constancy ($(s^2)_{in} = (s_{in})^2$ and $(s^2)_{out} = (s_{out})^2$) deviates by 28 $\%$ (see Table (4.2)).

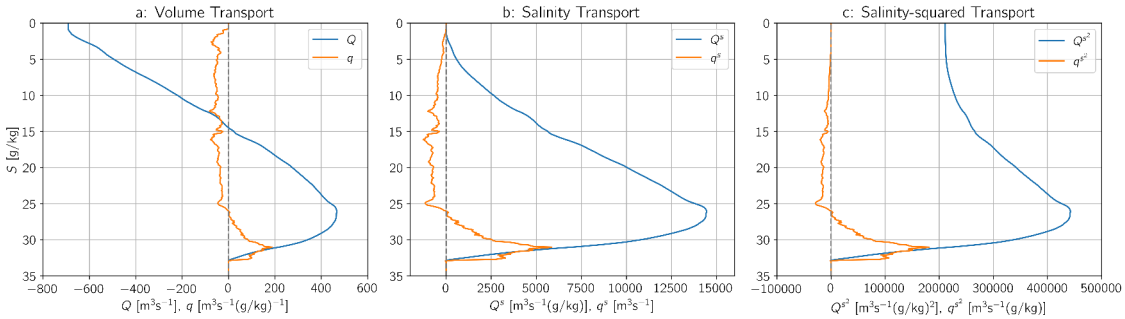

Figure 4.2.: Exchange flow profiles in salinity class S for monochromatic semi-diurnal tidal forcing taken averaged over 10 tidal periods. a) blue showing volume transport $Q(S)$ and orange showing volume transport per salinity class $q(S)$. b) blue showing salinity transport $Q^s(S)$ and orange showing salinity transport per salinity class $q^s(S)$. c) blue showing salinity-squared transport $Q^{s^2}(S)$ and orange showing salinity-squared transport per salinity class $q^{s^2}(S)$.

Transport Values	Variable	Value	
Volume transport inflow	Q_{in}	466.291	m^3s^{-1}
Volume transport outflow	Q_{out}	-1157.217	m^3s^{-1}
Salinity transport inflow	Q^s_{in}	14442.528	m^3s^{-1}(g/kg)
Salinity transport outflow	Q^s_{out}	-14439.466	m^3s^{-1}(g/kg)
Salt inflow	s_{in}	30.973	g/kg
Salt outflow	s_{out}	12.477	g/kg
Salinity-squared transport inflow	$Q^{s^2}_{in}$	442402.475	$m^3s^{-1}(g/kg)^2$
Salinity-squared transport outflow	$Q^{s^2}_{out}$	-231504.461	$m^3s^{-1}(g/kg)^2$
Salt-squared inflow	s^2_{in}	948.767	$(g/kg)^2$
Salt-squared outflow	s^2_{out}	200.052	$(g/kg)^2$
Volume storage term	$\langle V_{stor} \rangle$	9.074	$m^s s^{-1}$
Salinity storage term	$\langle S_{stor} \rangle$	3.062	$m^s s^{-1}$(g/kg)
Salinity-squared storage term	$\langle (S^2)_{stor} \rangle$	124.302	$m^s s^{-1}(g/kg)^2$

Table 4.1.: Exchange flow quantities of estuary forced with monochromatic semi-diurnal averaged over 10 tidal periods at transect B.

Further discussing the isohaline mixing, the integrated mixing $M(S)$ almost follows the theoretical curve until the salinity isohaline not leaving the estuary, see Fig 4.3a. Whereas in Fig 4.3b, the mixing per salinity class $m(S)$ obeys the theoretical curve until the salinity reaches 23 g/kg, which is the maximum salinity not reaching the open

boundary. The integrated isohaline mixing $M(S)$ is smoother and does not deviate much from the theoretical curve as it is the integrated from mixing per salinity class $m(S)$, all the fluctuations add-up to make the curve smoother. The integrated numerical mixing M^{num} and numerical mixing per salinity class m^{num} increases at high salinity classes and are dominant from 30 g/kg, where resolution of the estuary is coarser at the opening. These high salinity classes occur at these larger grid cells.

Mixing Estimates	Variable	Value[m^{s}s^{-1}(g/kg)^2]
Mixing	$\langle M \rangle$	210773.711
Physical mixing	$\langle M^{\text{phy}} \rangle$	198288.832
Numerical mixing	$\langle M^{\text{num}} \rangle$	12484.879
Exact mixing relation	$\langle M_e \rangle$	210773.711
Mixing relation (assuming constancy and periodicity)	$\langle M_{cp} \rangle$	270532.624

Table 4.2.: Mixing estimates averaged over 10 tidal periods for monochromatic semi-diurnal tide, rounded up to three decimal places.

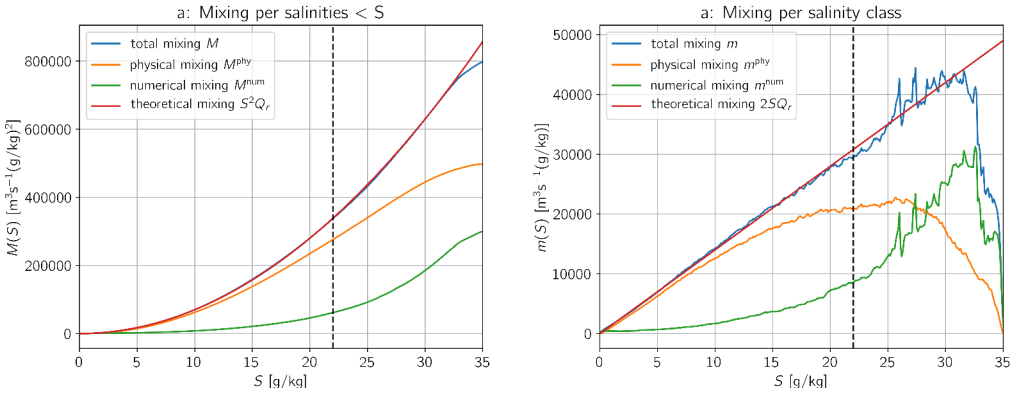

Figure 4.3.: Numerical estuary model forced with monochromatic semi-diurnal tides averaged over 10 tidal periods: a) tidally averaged mixing $M(S)$ (blue) and its decomposition integrated over all salinities $< S$ as function of S, including the theoretical curve (red), b) tidally averaged mixing per salinity class $m(S)$ (blue) and its decomposition as function of S, including the theoretical curve (red). The vertical hatched line indicates the maximum salinity (23 g/kg) reaching the open boundary.

The Fig 4.4a, shows the area of isohaline $a(S)$ and the volume of isohaline $v(S)$ which are the required inputs to calculate the effective diahaline diffusivity $\overline{K_n}$. Fig 4.4b represents the mean salinity gradient per salinity b^{-1}. For the salinities from 16

g/kg to 23 g/kg the gradient is above 10 (g/kg)m^{-1}, which means the isohaline in this salinity range is stretched with a thickness below 0.1 m per salinity class (see Fig 4.5). The effective diahaline diffusivity $\overline{K_n}$ increases linearly from 1·10 $^{-5}$ m^{2}s^{-1} for every 1 g/kg of salinity to a peak of 6·10 $^{-5}$ m^{2}s^{-1} at 7 g/kg and decreases again to 1·10 $^{-5}$ m^{2}s^{-1} at 23g/kg (see Fig 4.4c). And for salinities larger than 23 g/kg the $\overline{K_n}$ is nearly greater than 2·10 $^{-5}$ m^{2}s^{-1} with a peak diahaline diffusivity of 1·10 $^{-4}$ m^{2}s^{-1} is due to small salinity gradient and high isohaline volume.

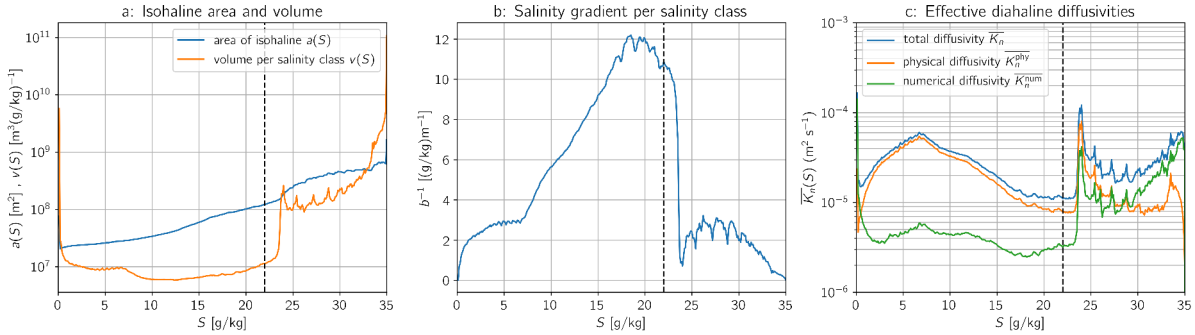

Figure 4.4.: Averaged over 10 tidal periods estuary forced with monochromatic semi-diurnal tides: a) area of isohaline $a(S)$, and volume per salinity class $v(S)$, b) averaged salinity gradient, b^{-1} resulting from $a(S)$ and $v(S)$, and c) effective physical, numerical and total diahaline diffusivity. The vertical dashes indicates the maximum salinity (23 g/kg) not reaching the open boundary.

The TEF-based and thickness-weighted salinity distributions are shown in Fig 4.5, taken at the center-line estuary (y=0). The TEF-based salinity distributions are taken from the Total Exchange flow (TEF) framework, where the isohaline position is indicated inside the water column for all locations (x,y), at every position of the salinity S has occurred during the averaging period. The thickness-weighted distribution has first been averaged on σ-layers and weighted over the changing water depth, then the averaged salinity values are associated with vertical averaged position of the respective σ-layers (for more details, see (Burchard et al., 2020, submitted) and Klingbeil et al. (2019)). As seen, the TEF-based isohalines are spread widely when compared with the thickness-weighted isohalines. For example, the isohaline $S = 15$ g/kg (marked in red) in TEF-based is twice long than the thickness-weighted. This is because, when a specific salinity appears in water column, the respective isohaline is stretched across the horizontal position. Which might not be seen in the thickness-weighted averaging. However, the isohaline are differently spread, the volume of isohalines are same for both the cases (see Burchard et al. (2020), submitted). Fig 4.6 shows the spatial

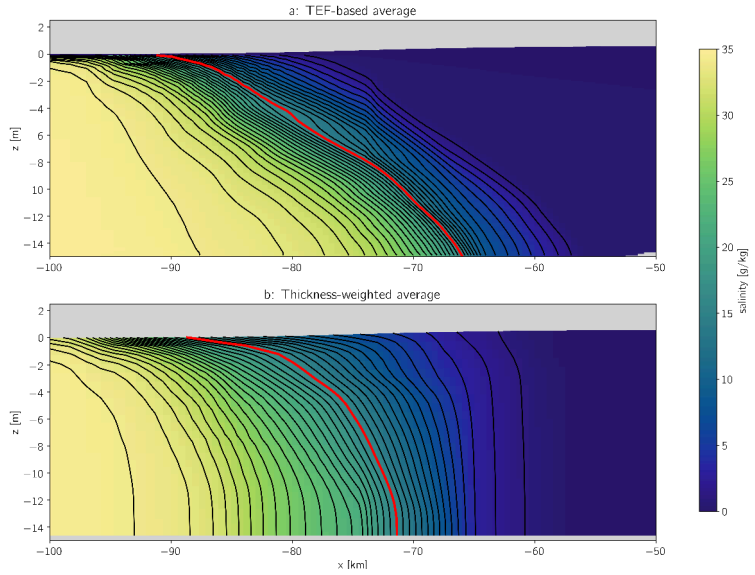

Figure 4.5.: Estuary simulation averaged over 10 tidal periods forced with monochromatic semi-diurnal tides: a) TEF-based averaged salinity distribution and isohaline positions, b) thickness-weighted averaged salinity distribution and isohaline positions. Both taken at the center-line of estuary (y=0), the isohaline are shown at ΔS =1 g/kg. The red-line indicates isohaline at $S = 15$ g/kg

distribution on diahaline diffusivity for $S = 15$ g/kg, as seen they reach high values at the inner channel. Also, the physical diahaline diffusivity values are dominant in the well resolved channel, as the outer mouth of estuary numerical values are significant due to the coarse resolution. These Fig (4.6) also helps to identify the mixing hotspots, i.e the inner channel where the diffusivity is high.

The Fig 4.7a, shows the mixing distribution over the salinity class and spatial longitudinal distance. Similarly, Fig 4.7b shows the mixing per salinity class integrated over the longitudinal distance and Fig 4.7c shows the mixing per longitudinal distance integrated over the salinity classes. As seen, most of the mixing takes place in the region of -90 km to -75 km, and also at higher salinity ranges. However, this doesn't follow any specific law.

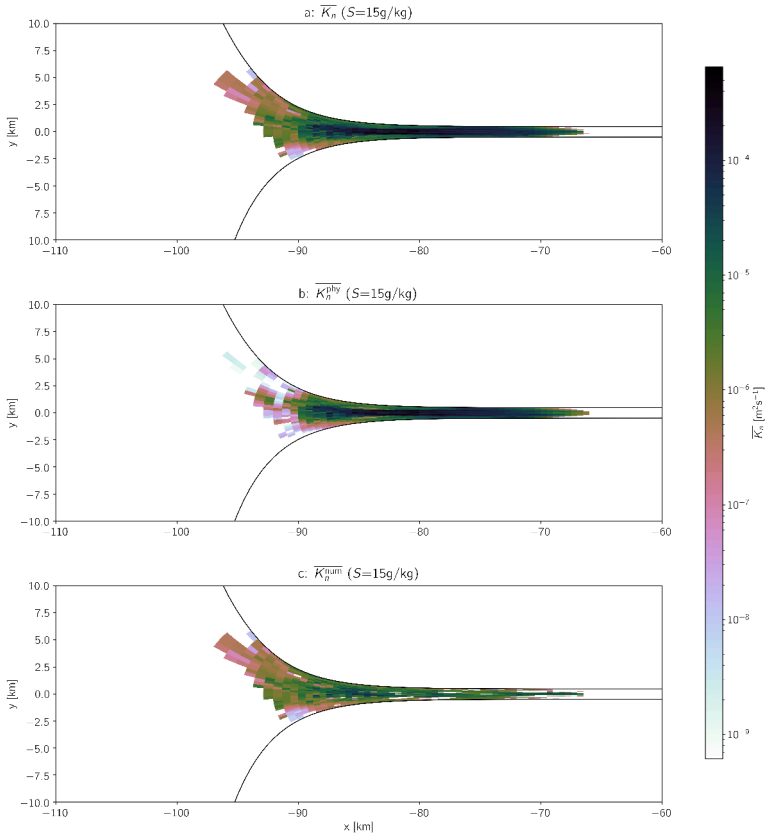

Figure 4.6.: Estuary simulation averaged over 10 tidal periods forced with monochromatic semi-diurnal tides: a) total, b) physical, c) numerical effective diahaline diffusivity for the isohaline $S = 15$g/kg spatial distributed (as a function (x,y)).

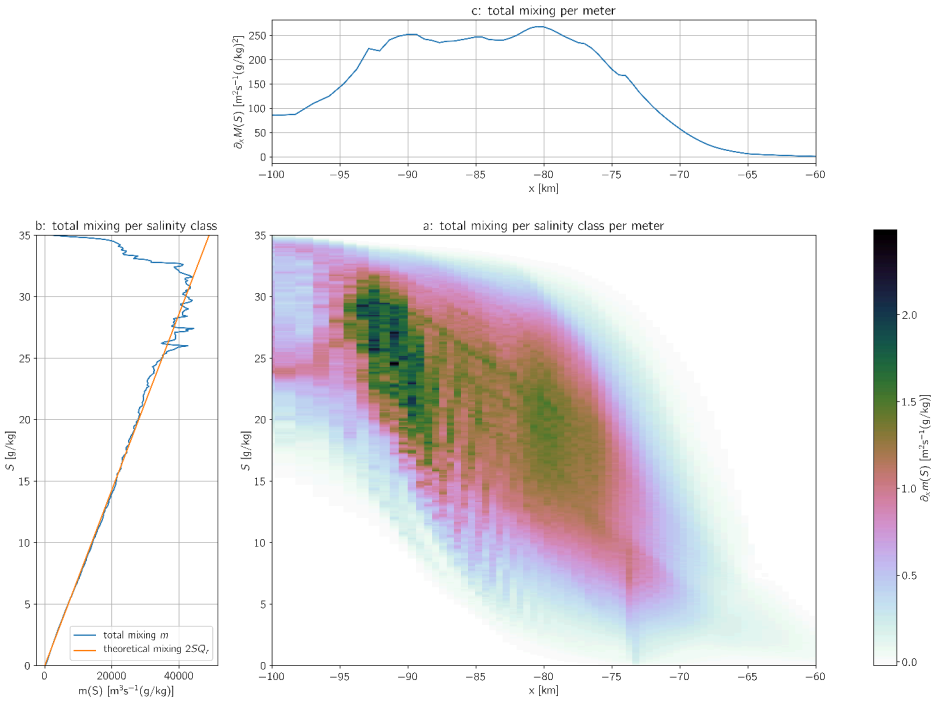

Figure 4.7.: Estuary simulation averaged over 10 tidal periods forced with monochromatic semi-diurnal tides: a) mixing per salinity class and longitudinal distance, $\partial_x m(S)$, b) mixing per salinity class $m(s) = \partial_s M(S)$ (integrated along longitudinal distance), c) mixing per longitudinal distance $\partial_x M(S)$ (integrated along salinity class).

4.2.2. Results of spring-neap tides

The exchange flow profiles seen in Fig 4.8, are investigated at the same transect B for the spring-neap cycles. These profiles are smoother compared to the exchange profiles of monochromatic semi-diurnal tidal forcing (see Fig 4.2) because these are averaged over 60 tidal periods (i.e two spring-neap cycles). Here also, inflow occurs around salinities $S > 26$ g/kg and is also a two-layered exchange flow. The average inflow and outflow transports also occur at the same salinities that is, inflows at ≈ 31 g/kg and outflows at ≈ 12g/kg. Even though, there is a loss in salinity and salinity-squared storage terms, the inflow and outflow volume, salinity and salinity-squared transports are similar to the monochromatic semi-diurnal tidal forcing values (see Table 4.3).

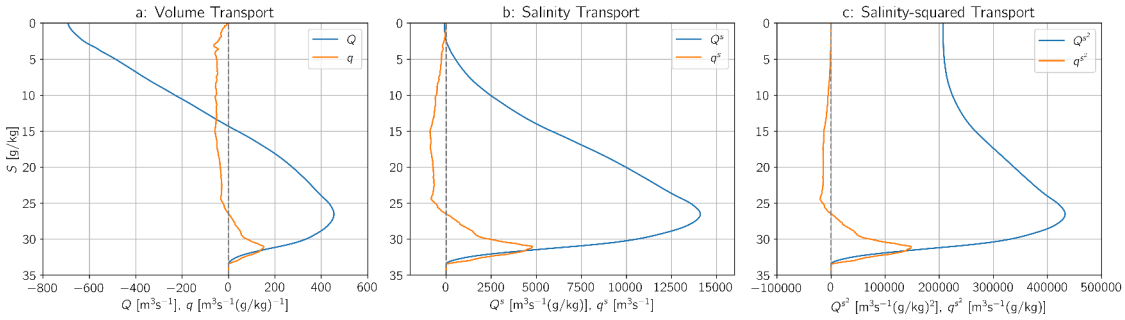

Figure 4.8.: Exchange flow profiles in salinity class S for spring-neap tidal cycle forcing taken averaged over two spring-neap cycles. a) blue showing volume transport $Q(S)$ and orange showing volume transport per salinity class $q(S)$. b) blue showing salinity transport $Q^s(S)$ and orange showing salinity transport per salinity class $q^s(S)$. c) blue showing salinity-squared transport $Q^{s^2}(S)$ and orange showing salinity-squared transport per salinity class $q^{s^2}(S)$.

The mixing estimates from the simulation $\langle M \rangle$ also obey the mixing value from the exact mixing relation $\langle M_e \rangle$. Similarly, the mixing relation $\langle M_{cp} \rangle$ assuming constancy and periodicity deviates by 28% (see Table 4.9). The universal law of estuarine mixing is also satisfied by the mixing quantified from the simulation, and is slightly deviated from the theoretical curve after 20 g/kg salinity class.

The isohaline volume and the isohaline area (see Fig 4.10a) are nearly same to that of the previous result of the monochromatic semi-diurnal tides, but are smoother after 25 g/kg salinity classes compared to the monochromatic tides. The salinity gradient b^{-1} increases linearly from 2 g/kg to a peak at 18 g/kg and drops after 20 g/kg (see

Transport Values	Variable	Value	
Volume transport inflow	Q_{in}	454.454	m^3s^{-1}
Volume transport outflow	Q_{out}	-1145.857	m^3s^{-1}
Salinity transport inflow	Q^s_{in}	14100.101	m^3s^{-1}(g/kg)
Salinity transport outflow	Q^s_{out}	-14187.554	m^3s^{-1}(g/kg)
Salt inflow	s_{in}	31.026	g/kg
Salt outflow	s_{out}	12.381	g/kg
Salinity-squared transport inflow	$Q^{s^2}_{in}$	432724.589	m^3s^{-1}(g/kg)^2
Salinity-squared transport outflow	$Q^{s^2}_{out}$	-225607.208	m^3s^{-1}(g/kg)^2
Salt-squared inflow	s^2_{in}	952.183	(g/kg)^2
Salt-squared outflow	s^2_{out}	196.889	(g/kg)^2
Volume storage term	$\langle V_{stor} \rangle$	8.597	$m^s s^{-1}$
Salinity storage term	$\langle S_{stor} \rangle$	-87.453	$m^s s^{-1}$(g/kg)
Salinity-squared storage term	$\langle (S^2)_{stor} \rangle$	-1436.440	$m^s s^{-1}$(g/kg)^2

Table 4.3.: Exchange flow quantities of estuary forced with spring-neap tidal cycle averaged over two spring-neap cycles periods at transect B.

Mixing Estimates	Variable	Value[$m^s s^{-1}$(g/kg)^2]
Mixing	$\langle M \rangle$	208553.866
Physical mixing	$\langle M^{\mathrm{phy}} \rangle$	197009.515
Numerical mixing	$\langle M^{\mathrm{num}} \rangle$	11544.351
Exact mixing relation	$\langle M_e \rangle$	208553.821
Mixing relation (assuming constancy and periodicity)	$\langle M_{cp} \rangle$	268909.604

Table 4.4.: Mixing estimates averaged over two spring-neap cycles, rounded up to three decimal places.

Fig 4.10b). Here, there are less salinity classes in a salinity gradient values more than 10 (g/kg)m^{-1} compared to the monochromatic tides. In Fig 4.10, the $\overline{K_n}$ also reaches a peak of 4·10 $^{-5}$ m^2s^{-1} at 5g/kg which is lesser than effective diahaline diffusivity of monochromatic tides. This can be the cause of averaging a complete spring-neap cycle (i.e, over a well mixed phase and weakly mixed phase). The Fig 4.11, shows the TEF-based and thickness weighed isohalines distributions, where, the TEF-based

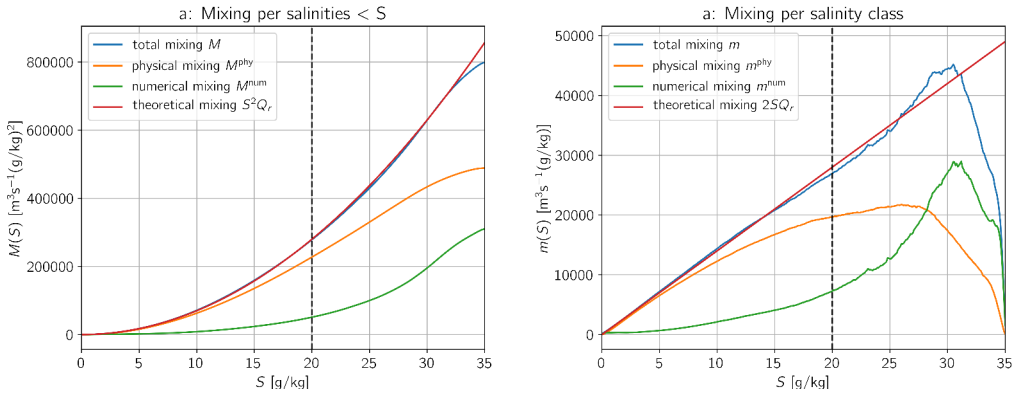

Figure 4.9.: Numerical estuary model averaged over two consecutive spring-neap cycles: a) tidally averaged mixing $M(S)$ (blue) and its decomposition integrated over all salinities $< S$ as function of S, including the theoretical curve (red), b) tidally averaged mixing per salinity class $m(S)$ (blue) and its decomposition as function of S, including the theoretical curve (red). The vertical hatched line indicates the maximum salinity (20 g/kg) reaching the open boundary.

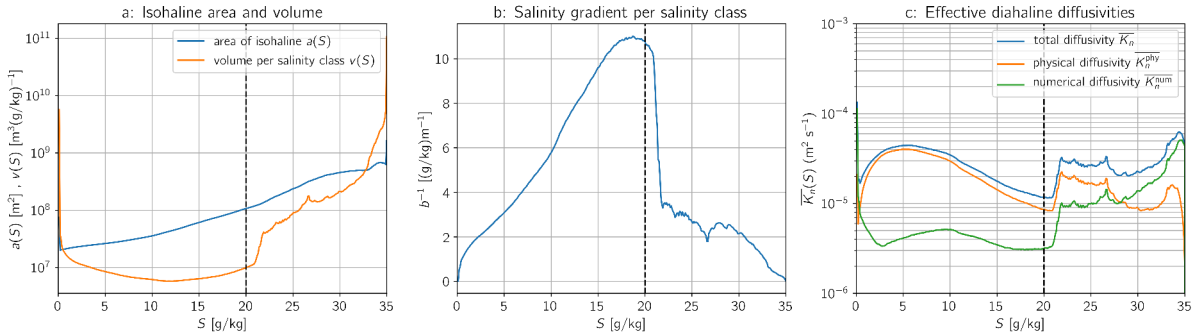

Figure 4.10.: Averaged over two consecutive spring-neap cycles: a) area of isohaline $a(S)$, and volume per salinity class $v(S)$, b) averaged salinity gradient, b^{-1} resulting from $a(S)$ and $v(S)$, and c) effective physical, numerical and total diahaline diffusivity. The vertical hatched line indicates the maximum salinity (20 g/kg) reaching the open boundary.

isohalines are nearly twice of the thickness weighted isohaline as discussed in the previous result section.

The spatial distribution of effective diahaline diffusivity of $S = 15$ g/kg is shown in Fig 4.12. Which also, shows the mixing hotspots at the inner channel region where the diffusivities are high. In Fig 4.13, also provide the information on high amount of mixing happening in region x= -95 km to -75 km. As mention before this plot is just to show the mixing distribution over longitudinal distance and salinity classes.

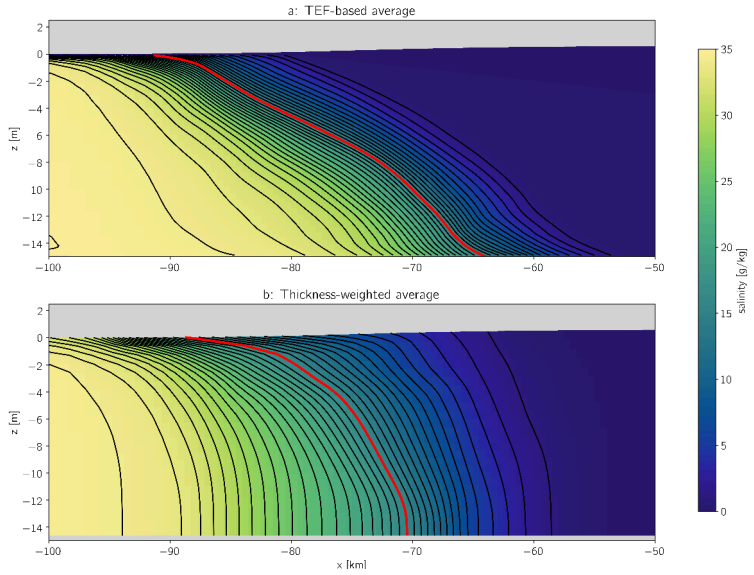

Figure 4.11.: Estuary simulation averaged over two consecutive spring-neap cycle: a) TEF-based averaged salinity distribution and isohaline positions, b) thickness-weighted averaged salinity distribution and isohaline positions. Both taken at the center-line of estuary (y=0), the isohaline are shown at ΔS =1 g/kg. The red-line indicates isohaline at S = 15 g/kg.

Now, looking at the exchange flows on every tide in the two investigated spring-neap cycles, Fig 4.14, the exchange flow are measured at the transect B (i.e, x= -80 km). The outflow salinities are around 10 g/kg to 15 g/kg with high salinity outflows at the end of neap tide and there is decrease in the outflow at spring tides (see Fig 4.14c and Fig 4.14d). The volume transport variations effected by the spring-neap cycle at transect B are seen in Fig 4.14b, the inflow fluctuate around 450 m^3s^{-1} and outflow volume around 1150 m^3s^{-1}, huge significant effect of tide cannot be seen from the plot.

However, the exchange flow variations computed at transect A (i.e, x= -90 km) are seen in Fig 4.15, the effect of tides can be seen over the exchange flow. There are high inflow and outflow transports happening at the neap tides and low transports at the spring tides, even for the net river discharge flowing out of estuary (see Fig 4.15b). There is high out flowing salinity at end of the neap tides and low at end of spring tides, where the peaks are at an offset of 5 days with respect to volume transport peaks. There is no considerable change in the inflow salinities as the transect A is closer to the open boundary. However, a slight peak in inflow salinities can be seen at the neap tides (see Fig 4.15c and Fig 4.15d). As the estuary is wider in transect A than transect B, which enabled a strong lateral exchange flow can be seen in Fig 4.1. Hence, this large

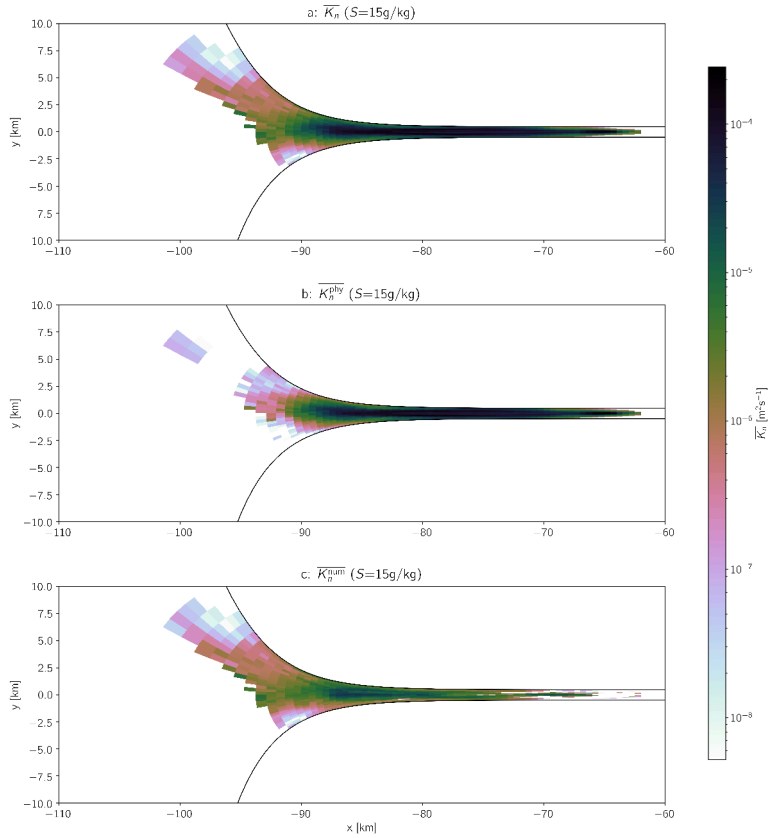

Figure 4.12.: Estuary simulation averaged over two consecutive spring-neap cycle: a) total, b) physical, c) numerical effective diahaline diffusivity for the isohaline $S = 15$g/kg spatial distributed (as a function (x,y)).

variations in the exchange flow can be seen at the transect A more compared to the transect B. The high saline water flowing out of estuary at the neap tides suggest that a high mixing occurs in neap tides compared to spring tides, which will be described in detail in next section.

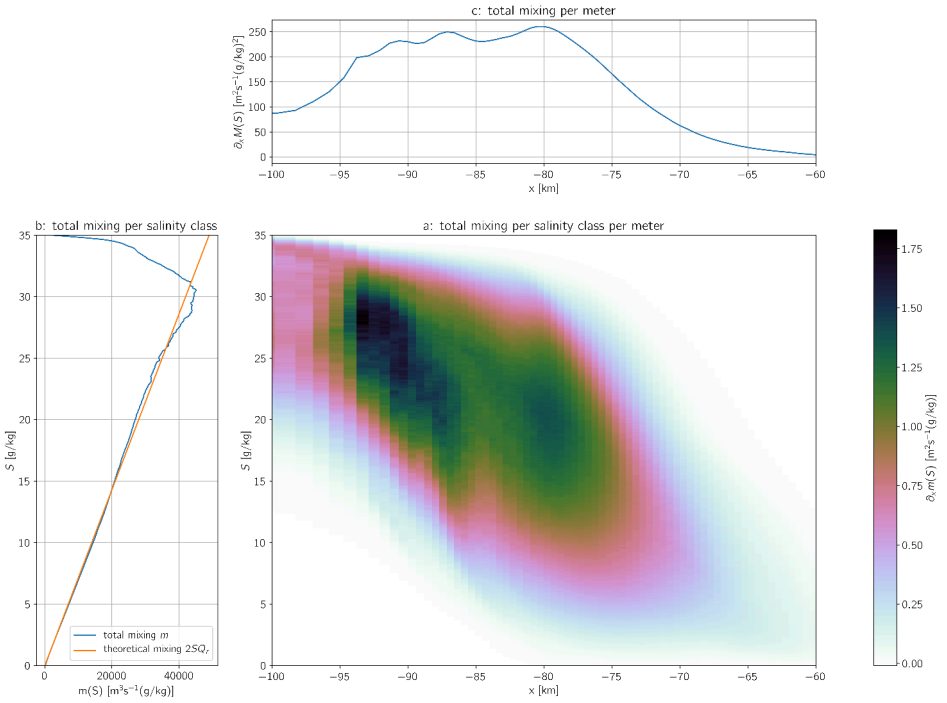

Figure 4.13.: Estuary simulation averaged over two consecutive spring-neap cycle: a) mixing per salinity class and longitudinal distance, $\partial_x m(S)$, b) mixing per salinity class $m(s) = \partial_s M(S)$ (integrated along longitudinal distance), c) mixing per longitudinal distance $\partial_x M(S)$ (integrated along salinity class).

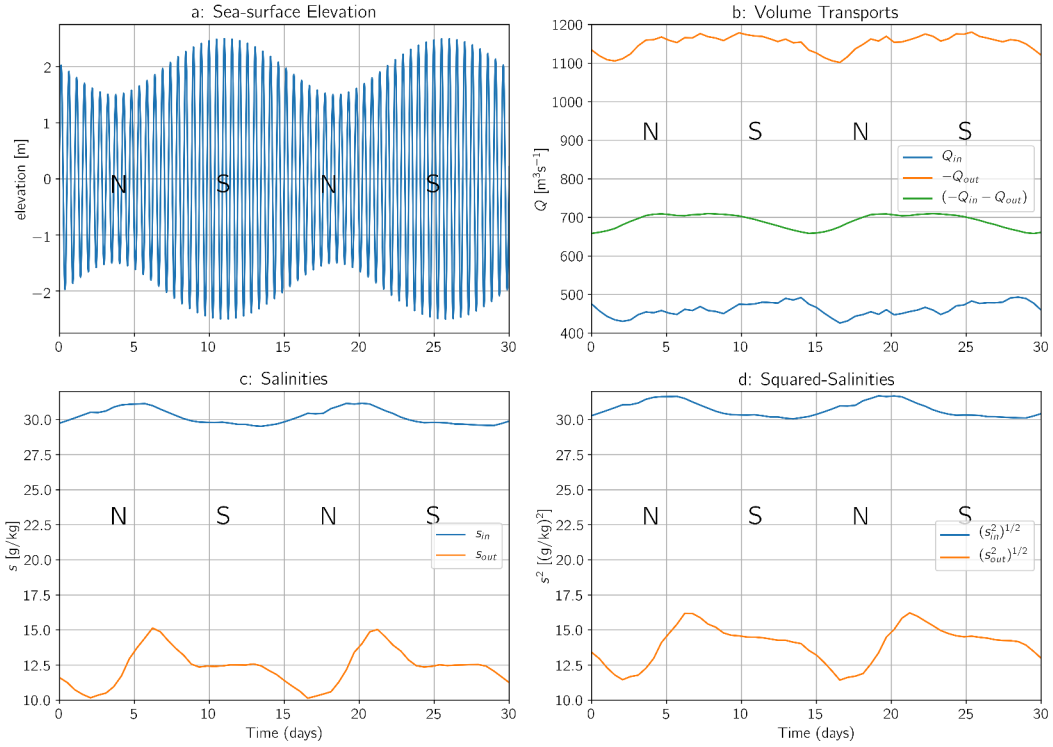

Figure 4.14.: Tidally averaged inflow and outflow transports in two consecutive spring-neap cycle: a) sea-surface elevation at open-boundary b) inflow and outflow volume transports c) salinities flowing into and out of estuary d) squared-salinities flowing in and out of estuary. All taken at transect B. S-represents spring tide and N-represents neap tide.

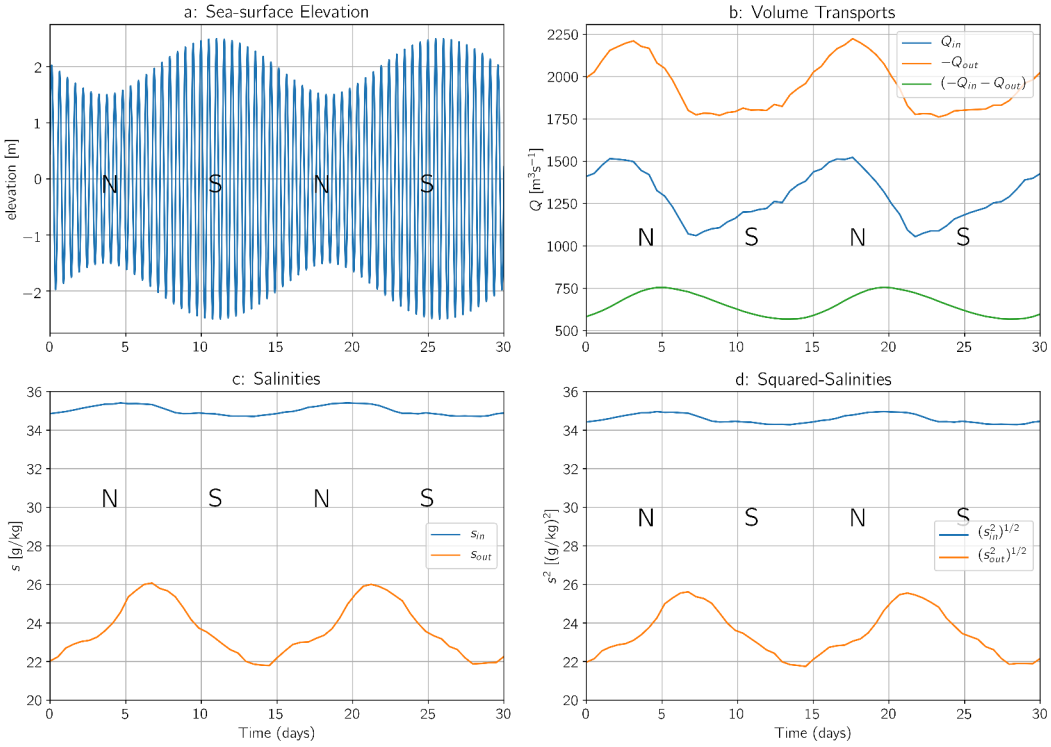

Figure 4.15.: Tidally averaged inflow and outflow transports in two consecutive spring-neap cycle: a) sea-surface elevation at open-boundary b) inflow and outflow volume transports c) salinities flowing into and out of estuary d) squared-salinities flowing in and out of estuary. All taken at transect A. S-represents spring tide and N-represents neap tide.

4.2.3. Results of spring-neap tides (averaged over weak tides and strong tides)

In the previous section, the results are discussed over a complete spring-neap cycle. In this section, the dynamics of estuary are presented which are concentrated over the weak tides (neap tides) and strong tides (spring tides) in the spring-neap cycle.

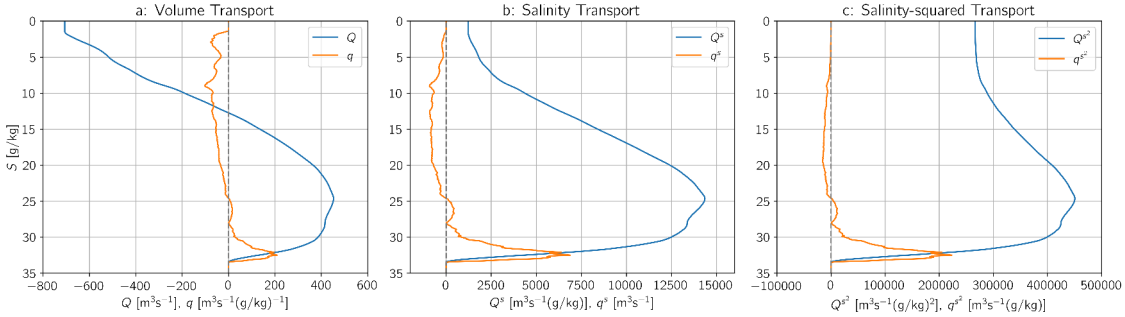

Figure 4.16.: Exchange flow profiles in salinity class S for spring-neap tidal forcing taken averaged over 10 consecutive weak tides. a) blue showing volume transport $Q(S)$ and orange showing volume transport per salinity class $q(S)$. b) blue showing salinity transport $Q^s(S)$ and orange showing salinity transport per salinity class $q^s(S)$. c) blue showing salinity-squared transport $Q^{s^2}(S)$ and orange showing salinity-squared transport per salinity class $q^{s^2}(S)$.

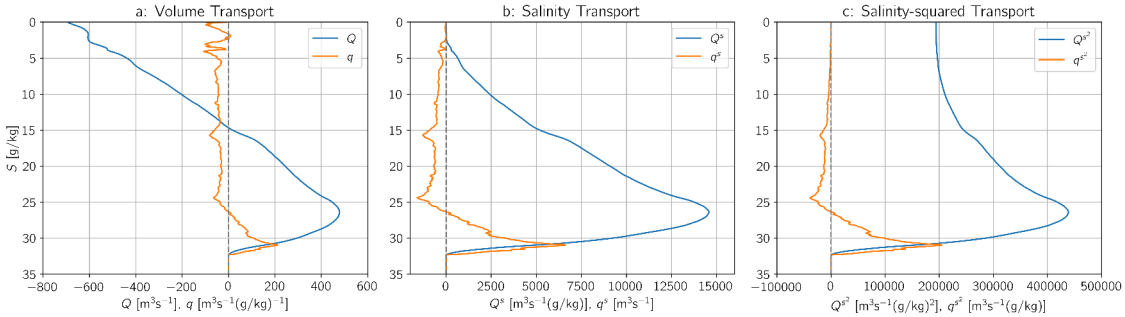

Figure 4.17.: Exchange flow profiles in salinity class S for spring-neap tidal forcing taken averaged over 10 consecutive strong tides. a) blue showing volume transport $Q(S)$ and orange showing volume transport per salinity class $q(S)$. b) blue showing salinity transport $Q^s(S)$ and orange showing salinity transport per salinity class $q^s(S)$. c) blue showing salinity-squared transport $Q^{s^2}(S)$ and orange showing salinity-squared transport per salinity class $q^{s^2}(S)$.

The exchange flow profiles are drawn for 10 tidal averaged consecutive weak tides (see Fig 4.16) and 10 tidal averaged consecutive strong tides (see Fig 4.17) of spring-

Transport Values	Variable	Averaged over 10 consecutive		Units
		Strong Tide	Weak Tide	
Volume transport inflow	Q_{in}	478.744	452.676	m^3s^{-1}
Volume transport outflow	Q_{out}	-1168.904	-1159.411	m^3s^{-1}
Salinity transport inflow	Q^s_{in}	14574.244	14352.244	m^3s^{-1}(g/kg)
Salinity transport outflow	Q^s_{out}	-14594.855	-13133.345	m^3s^{-1}(g/kg)
Salt inflow	s_{in}	30.442	31.705	g/kg
Salt outflow	s_{out}	12.485	11.327	g/kg
Salinity-squared transport inflow	$Q^{s^2}_{in}$	438750.708	450689.828	m^3s^{-1}(g/kg)^2
Salinity-squared transport outflow	$Q^{s^2}_{out}$	-244431.956	-184346.985	m^3s^{-1}(g/kg)^2
Salt-squared inflow	s^2_{in}	916.460	995.612	(g/kg)^2
Salt-squared outflow	s^2_{out}	209.112	159.001	(g/kg)^2
Volume storage term	$\langle V_{stor} \rangle$	9.840	-6.734	$m^s s^{-1}$
Salinity storage term	$\langle S_{stor} \rangle$	-0.006	0.119	$m^s s^{-1}$(g/kg)
Salinity-squared storage term	$\langle (S^2)_{stor} \rangle$	0.013	-13.261	$m^s s^{-1}$(g/kg)^2

Table 4.5.: Exchange flow quantities of estuary forced with spring-neap cycle averaged over 10 consecutive spring tides and 10 consecutive neap tides at transect B.

neap cycles over the transect B. Seeing from the profiles, inflow occurs at salinities nearly $S > 26$ g/kg for the strong tides and $S > 24$ g/kg for the weak tides, where, the inflow occurs at $S > 26$ g/kg for a complete spring-neap cycle (see 4.2.2). As expected, the inflow volume transport is higher for the strong tides compared to the weak tides with a difference of 26 $m^3s{-}1$. Also, the inflow and outflow salinities differ by 1 g/kg between the strong and weak tides (see Table 4.5).

Now comparing the mixing estimates from the model and from relations (see Table 4.6), the exact mixing relation $\langle M_e \rangle$ deviates by 0.3 $\%$ for the strong tides and -16 $\%$ for the weak tides. This error in estimation of mixing from the exact mixing relation can be due to individual strong tides or weak tides, which are not in equilibrium compared the complete spring-neap cycle. When assuming constancy and periodicity $\langle M_{cp} \rangle$, the mixing is estimated with an error of 36 $\%$ for the strong tides and -2 $\%$ for the weak tides. There is no particular hypothesis that can de drawn from these estimates.

However, inspecting the universal mixing law for these weak tides (Fig 4.18) and strong tides (Fig 4.19) individually in comparison with the theoretical curve, there is

Mixing Estimates	Variable	Strong Tide $[m^s s^{-1}(g/kg)^2]$	Weak Tide $[m^s s^{-1}(g/kg)^2]$
Mixing	$\langle M \rangle$	194371.483	258326.862
Physical mixing	$\langle M^{\mathrm{phy}} \rangle$	186542.361	238835.259
Numerical mixing	$\langle M^{\mathrm{num}} \rangle$	7829.122	19491.602
Exact mixing relation	$\langle M_e \rangle$	195130.354	216318.911
Mixing relation (assuming constancy and periodicity)	$\langle M_{cp} \rangle$	266072.897	251401.681

Table 4.6.: Mixing estimates averaged over 10 consecutive strong tides and 10 consecutive weak tides, rounded up to three decimal places.

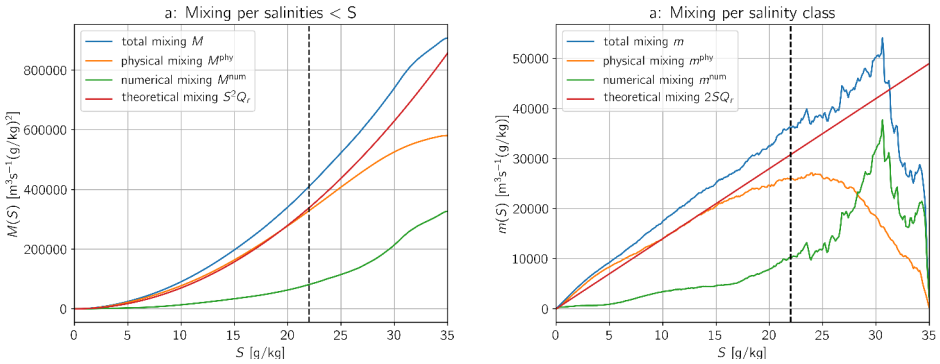

Figure 4.18.: Numerical estuary model forced with spring-neap cycle averaged over 10 consecutive weak tides: a) tidally averaged mixing $M(S)$ (blue) and its decomposition integrated over all salinities $< S$ as function of S, including the theoretical curve (red), b) tidally averaged mixing per salinity class $m(S)$ (blue) and its decomposition as function of S, including the theoretical curve (red). The vertical hatched line indicates salinity class (23 g/kg) in comparison with results of monochromatic semi-diurnal tides.

more mixing estimated in the weak tides and less mixing in the strong tides. This seems counter-intuitive as the stronger tides have less mixing values than the weaker tides. It can be a reason that the estuary in strong tide phase is already in a well mixed phase due to the early spring tides and thus, less mixing in strong tides. Whereas, in weak tide phase the salinity gradients are increased due to weaker tidal stresses, this leads to more mixing. The Fig 4.20b and Fig 4.21b explains the salinity stratification. The salinity gradient is high in the weak tides overall compared to the spring tides, even though the stronger tides have a high peak ≈ 14 (g/kg)m^{-1} in salinity gradient and drop down to 1 (g/kg)m^{-1} at salinity 26 g/kg. The $\overline{K_n}$ in the weak tides reaches a peak

of 8·10 $^{-5}$ m^{2}s^{-1} at the initial salinities following a drop to 1·10 $^{-5}$ m^{2}s^{-1} at 20 g/kg salinity class and again reaches to peak of 1·10 $^{-4}$ m^{2}s^{-1} at the higher salinity classes of 33 g/kg (see Fig 4.20c). Whereas, in the strong tides $\overline{K_n}$ reaches a peak of 4·10 $^{-5}$ m^{2}s^{-1} at 5 g/kg salinity and drop to 7·10 $^{-6}$ m^{2}s^{-1} at salinity class 25 g/kg, and again reaches a peak of 1·10 $^{-4}$ m^{2}s^{-1} at salinity 27 g/kg (see Fig 4.21c). This implies, there is more diffusivity in weak tides as a result of high mixing than the strong tides.

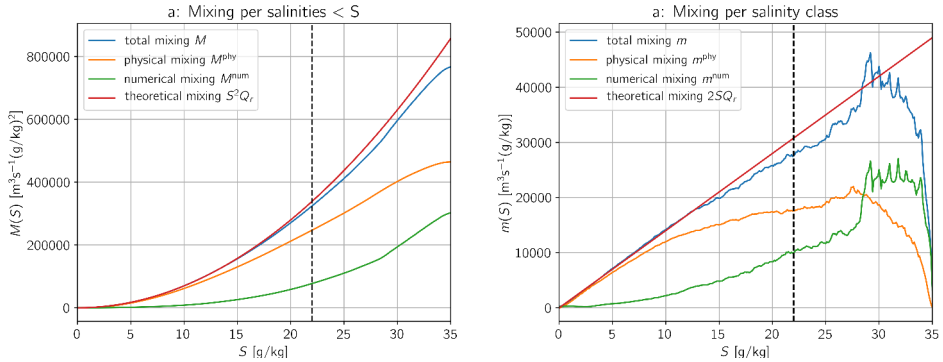

Figure 4.19.: Numerical estuary model forced with spring-neap cycle averaged over 10 consecutive strong tides: a) tidally averaged mixing $M(S)$ (blue) and its decomposition integrated over all salinities $< S$ as function of S, including the theoretical curve (red), b) tidally averaged mixing per salinity class $m(S)$ (blue) and its decomposition as function of S, including the theoretical curve (red). The vertical hatched line indicates salinity class (23 g/kg) in comparison with results of monochromatic semi-diurnal tides.

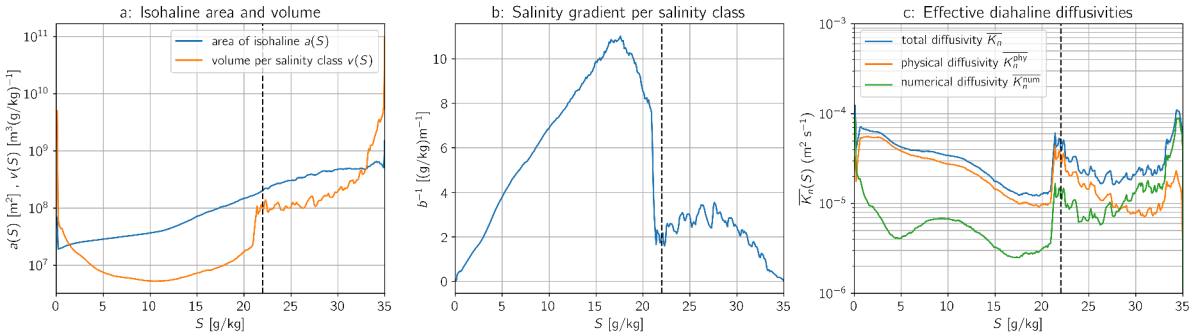

Figure 4.20.: Averaged over 10 consecutive weak tides, estuary forced with spring-neap cycle: a) area of isohaline $a(S)$, and volume per salinity class $v(S)$, b) averaged salinity gradient, b^{-1} resulting from $a(S)$ and $v(S)$, and c) effective physical, numerical and total diahaline diffusivity. The vertical hatched line indicates salinity class (23 g/kg) in comparison with results of monochromatic semi-diurnal tides.

The TEF-based and thickness-weighed averaged salinity distributions also show that the salinity gradient are high for weak tides to that of strong tides. The isohaline 15

g/kg is stretched wide for the weak tide compared to the strong tide. Also, saline water intrusion is more into the estuary at weak tide phase than the strong tide phase (see Fig 4.22 and Fig 4.23).

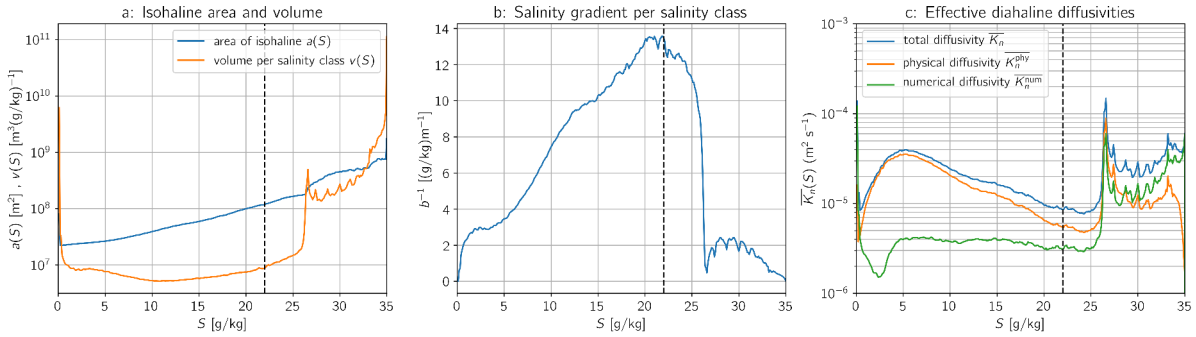

Figure 4.21.: Averaged over 10 consecutive strong tides, estuary forced with spring-neap cycle: a) area of isohaline $a(S)$, and volume per salinity class $v(S)$, b) averaged salinity gradient, b^{-1} resulting from $a(S)$ and $v(S)$, and c) effective physical, numerical and total diahaline diffusivity. The vertical hatched line indicates salinity class (23 g/kg) in comparison with results of monochromatic semi-diurnal tides.

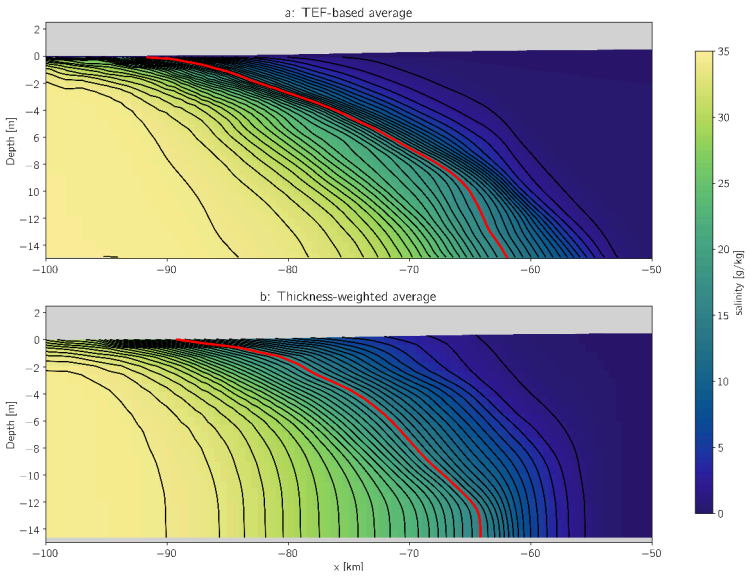

Figure 4.22.: Estuary simulation averaged over 10 consecutive weak tides forced with spring-neap cycle: a) TEF-based averaged salinity distribution and isohaline positions, b) thickness-weighted averaged salinity distribution and isohaline positions. Both taken at the center-line of estuary (y=0), the isohaline are shown at ΔS =1 g/kg. The red-line indicates isohaline at S = 15 g/kg

Looking at the spatial distribution of diahaline diffusivity for S = 15 g/kg in the weak tides, the diahaline diffusivity is higher and covers more region from x = -61 km

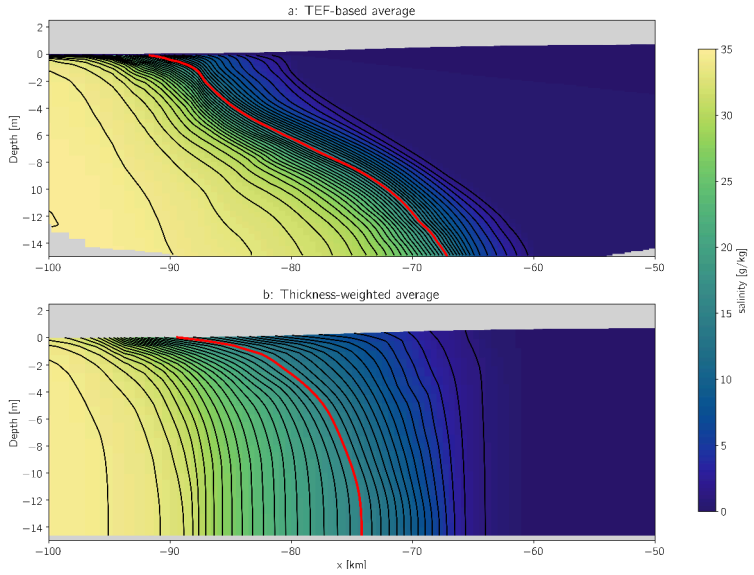

Figure 4.23.: Estuary simulation averaged over 10 consecutive strong tides forced with spring-neap cycle: a) TEF-based averaged salinity distribution and isohaline positions, b) thickness-weighted averaged salinity distribution and isohaline positions. Both taken at the center-line of estuary (y=0), the isohaline are shown at ΔS =1 g/kg. The red-line indicates isohaline at S = 15 g/kg

to -100 km (see Fig 4.24), to that of the strong tides which only covers a region of x = -97 km to -68 km and also has lesser magnitude (see Fig 4.25). This justifies that the weak tides have more salinity gradient than the stronger tides. In both the cases diahaline diffusivities are higher at the inner channel.

Considering, the mixing distribution over longitudinal distance and salinity classes for the weaker tides, they have a single mixing spot at salinity range S = 10 g/kg to 30 g/kg at the longitudinal distances x = -95 km to -75 km with a higher magnitude can be seen Fig 4.26. Whereas, the strong tides have two mixing spots, a strong mixing spot at x= -95 km to -90 km and a second mixing spot at x= -80 km to -75 km. Note that, the magnitude of mixing is lower in strong tides than compared to weak tides. From this, one can say that there is more mixing at weak tide phase as it is in less mixed state, and less mixing in strong tides as the estuary is already in well mixed state. Also, note that, the high saline water is induced deeper in the weak tides than the strong tides.

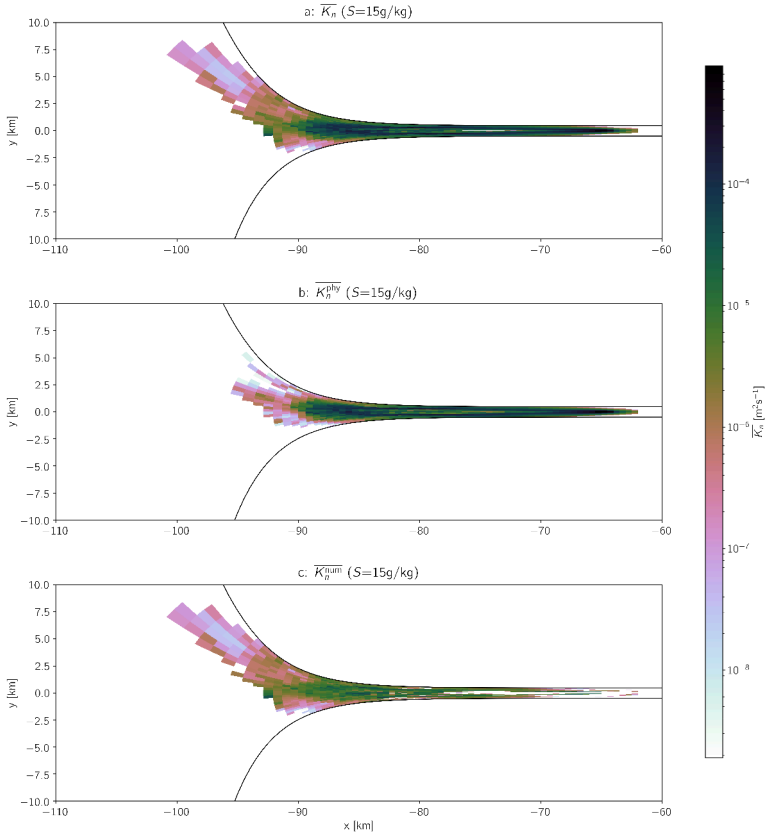

Figure 4.24.: Estuary simulation averaged over 10 consecutive weak tides forced with spring-neap cycle: a) total, b) physical, c) numerical effective diahaline diffusivity for the isohaline $S = 15$g/kg spatial distributed (as a function (x,y)).

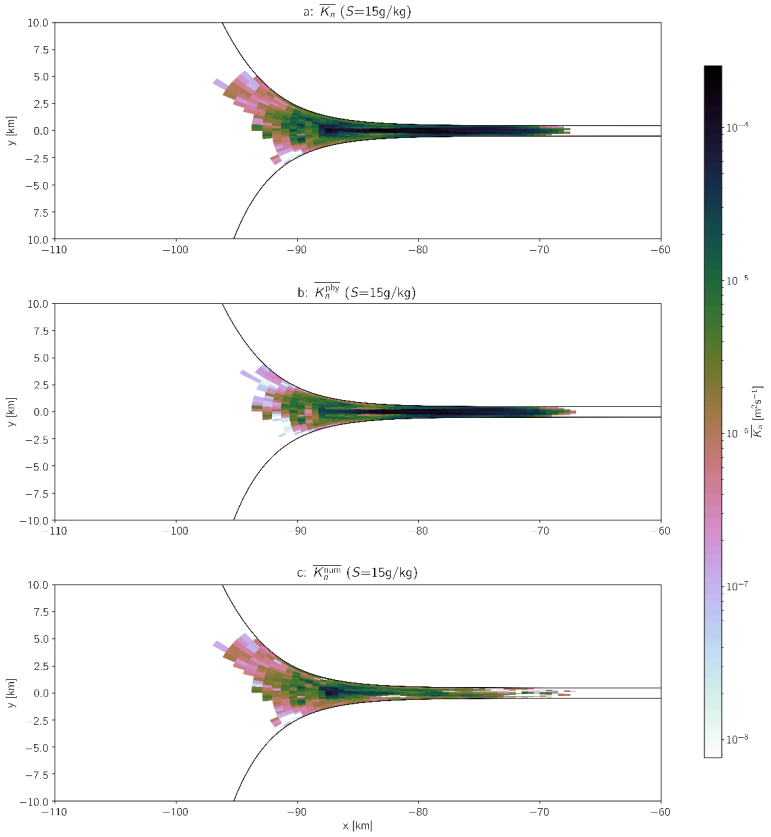

Figure 4.25.: Estuary simulation averaged over 10 consecutive strong tides forced with spring-neap cycle: a) total, b) physical, c) numerical effective diahaline diffusivity for the isohaline $S = 15$g/kg spatial distributed (as a function (x,y)).

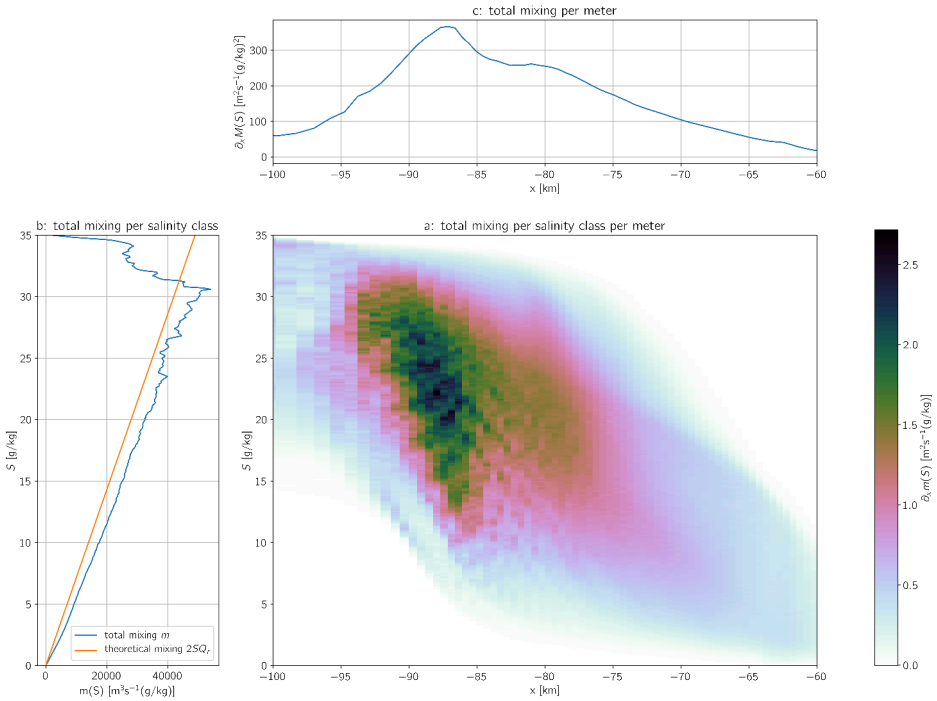

Figure 4.26.: Estuary simulation averaged over 10 consecutive weak tides forced with spring-neap cycle: a) mixing per salinity class and longitudinal distance, $\partial_x m(S)$, b) mixing per salinity class $m(s) = \partial_s M(S)$ (integrated along longitudinal distance), c) mixing per longitudinal distance $\partial_x M(S)$ (integrated along salinity class).

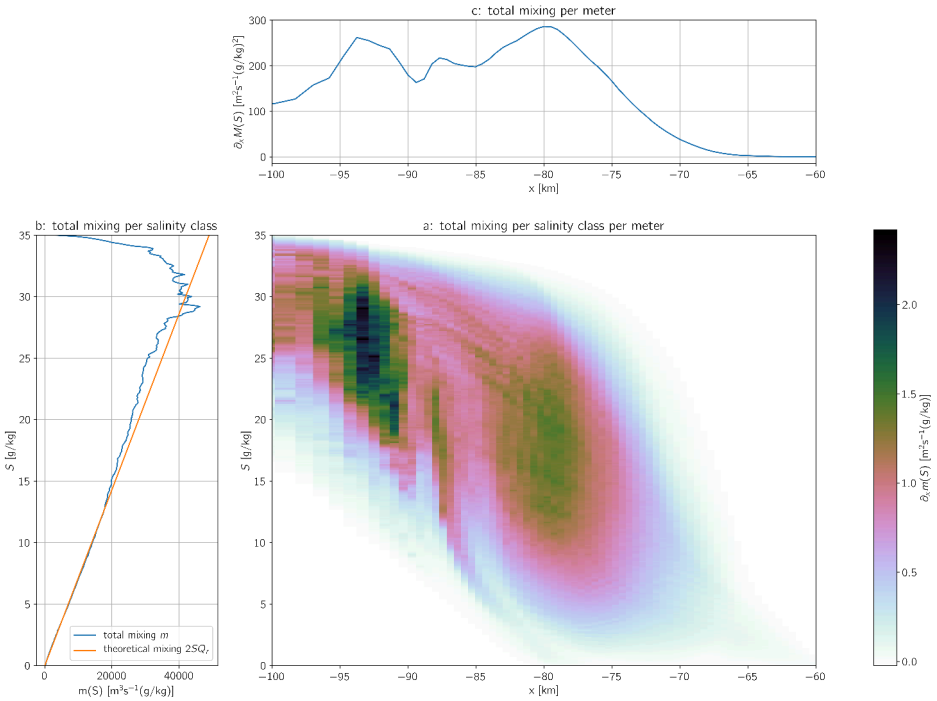

Figure 4.27.: Estuary simulation averaged over 10 consecutive strong tides forced with spring-neap cycle: a) mixing per salinity class and longitudinal distance, $\partial_x m(S)$, b) mixing per salinity class $m(s) = \partial_s M(S)$ (integrated along longitudinal distance), c) mixing per longitudinal distance $\partial_x M(S)$ (integrated along salinity class).

Chapter 5.

Conclusions

The mixing is quantified for this three-dimensional estuary numerical model. The presented study shows, the mixing computed from the model perfectly equals the mixing calculated using the Exact Mixing relation M_e derived by Burchard et al. (2019), and the simple mixing relation M_{cp} by MacCready et al. (2018) shows an error of 28$\%$ for both the cases of monochromatic semi-diurnal tides and spring-neap cycle. Where, the error percentage is higher than the two-dimensional estuary model tested in Burchard et al. (2019). For the analysis around weak tides and strong tides, the mixing estimates from the relations cannot be compared to the mixing computed from model as the budgets of weak tides and strong tides are not properly closed.

In the isohaline mixing, the monochromatic semi-diurnal tides and spring-neap cycle follow the theoretical curve. Also, obey the universal law of mixing until the open boundary as suggested by Burchard (2020). In the analysis of weak tides and strong tides, the weak tides have more mixing than the excepted theoretical curve and strong tide have lesser mixing. This can also be justified as the weak tide phase in the spring-neap cycle having more salinity gradient and deep intrusions of saline water to the estuary compared to that of the strong tide phase. The effective diahaline diffusivity is a newly introduce method by Burchard et al. (2020),submitted. This methods help to identify the mixing spots in the estuary, which are shown for this presented numerical model. The mixing is mainly happening around the inner channel than that of the mouth (for more details see chapter 4).

Further more, if a keen look is taken at the exchange flow and mixing at individual tide in the spring-neap cycle, there is more mixing happening at the neap tides in comparison with spring tides. Hence, resulting in high salinity outflows at the end of the neap tides. Where as, from the results presented by MacCready et al. (2018) there is more mixing and high salinity outflows at the spring. This might be a reason

that MacCready et al. (2018) used weaker tidal forcing and high river discharge in comparison with the forcing applied in this thesis study.

Appendix A.

Properties of Reynolds Averaging

1. Average of fluctuation:
$$\langle X' \rangle = 0$$

2. Double averages:
$$\langle \langle X \rangle \rangle = \langle X \rangle$$

3. Linearity:
$$\langle X + \lambda Y \rangle = \langle X \rangle + \lambda \langle Y \rangle$$

4. Derivatives:
$$\langle \partial_t X \rangle = \partial_t \langle X \rangle$$

5. Product average:
$$\langle X \langle Y \rangle \rangle = \langle X \rangle \langle Y \rangle$$

6. Average of fluctuations product:
$$\langle X'Y' \rangle \neq 0$$

Appendix B.

Salinity Variance Squared Equation

Following is the derivation of salinity variance squared equation (3.9), re-writing $s = \bar{s} + s'$ as $s' = s - \bar{s}$, squaring and differentiating with respect to time t,

$$\begin{aligned} \partial_t (s - \bar{s})^2 &= \partial_t s^2 - 2\partial_t (s\bar{s}) + \partial_t \bar{s}^2 \\ &= \partial_t s^2 - 2\bar{s}\partial_t s - 2(s - \bar{s})\partial_t \bar{s} \\ &= \partial_t s^2 - 2\bar{s}\partial_t s - 2s'\partial_t \bar{s} \ . \end{aligned} \tag{B.1}$$

From salinity-squared equation (3.4), the term can be re-arranged as,

$$\partial_t s^2 = -\partial_n (s^2 u_n) + \partial_n (K \partial_n s^2) - 2K(\partial_n s)^2 \ . \tag{B.2}$$

Multiplying $2\bar{s}$ with salinity equation (2.19),

$$2\bar{s}\partial_t s = -2\bar{s}\partial_n (s u_n) + 2\bar{s}\partial_n (K \partial_n s) \ . \tag{B.3}$$

Substituting (B.2) and (B.3) in equation (B.1), results as follows:

$$\begin{aligned} \partial_t (s - \bar{s})^2 &= -\partial_n (s^2 u_n) + \partial_n (K \partial_n s^2) - 2K(\partial_n s)^2 \\ &\quad + 2\bar{s}\partial_n (s u_n) - 2\bar{s}\partial_n (K \partial_n s) \\ &= -\partial_n (s^2 u_n) - \partial_n (K \partial_n s^2) - 2K(\partial_n s)^2 - 2s'\partial_t \bar{s} \ , \end{aligned} \tag{B.4}$$

using equation (3.5) and re-arranging the terms as,

$$\partial_t s'^2 + \partial_n (s'^2 u_n) - \partial_n (K \partial_n s'^2) = -\chi^s - 2s' \partial_t \bar{s} \ . \tag{B.5}$$

Nomenclature

$(S'^2)_{stor}$ storage term for salinity variance

$(S^2)_{stor}$ storage term for salinity-squared

$\bar{\eta_x}$ temporally averaged surface elevation gradient

χ^s local salinity mixing per unit volume

ϵ dissipation rate of k

η surface height

ν kinematic viscosity

ν^s molecular diffusivity of salt

ν_t turbulent viscosity / eddy viscosity

ν'_t eddy diffusivity of salt

Ω_j Coriolis force

ρ density of water

ρ_0 reference density

τ^b bottom stress tensor

τ^s surface stress tensor

a isohaline area

$A(S)$ cross-section with salinity s higher than S

b isohaline thickness

c_μ non-dimensional constant

f Coriolis parameter

F^c flux of tracer c

F^{s^2} effective squared salinity flux

F^s salinity flux

g acceleration due to gravity

H bottom depth

k turbulent kinetic energy

K_n effective diahaline diffusivity

$M(S)$ integrated mixing in volume $V(S)$

$m(S)$ mixing per salinity in isohaline S

M^{num} numerical mixing

M^{phy} physical mixing

M_{cp} mixing (assuming periodicity and constancy)

M_e exact mixing

n outward normal vector

P pressure

$Q^c(S)$ incoming transport of c through cross-section $A(S)$

$q^c(S)$ incoming boundary flux of c per salinity class

Q_{in} inflow volume transport

Q_{out} outflow volume transport

Q_r river discharge

S isohaline at salinity S

s_{in}^2 salinity-squared of inflow

s_{out}^2 salinity-squared of outflow

s_{in} salinity of inflow

s_{out} salinity of outflow

S_{stor} storage term for salinity

u velocity

u_r residual run-off velocity

v volume per salinity class

$V(S)$ volume of estuary including all salinities $s \leq S$

V_{stor} storage term for volume

Bibliography

Burchard, H., 2020. A universal law of estuarine mixing. Journal of Physical Oceanography 50 (1), 81–93.

Burchard, H., Bolding, K., 2001. Comparative analysis of four second-moment turbulence closure models for the oceanic mixed layer. J. Phys. Oceanogr. 31, 1943–1968.

Burchard, H., Bolding, K., 2002. GETM: A General Estuarine Transport Model; Scientific Documentation. European Commission, Joint Research Centre, Institute for Environment and Sustainability.

Burchard, H., Bolding, K., Feistel, R., Gräwe, U., Klingbeil, K., MacCready, P., Mohrholz, V., Umlauf, L., van der Lee, E. M., 2018. The knudsen theorem and the total exchange flow analysis framework applied to the baltic sea. Progress in Oceanography 165, 268–286.

Burchard, H., Gräwe, U., Klingbeil, K., Koganti, N., Lange, X., Lorenz, M., 2020. Effective diahaline diffusivities in estuaries. Journal of Physical Oceanography[Submitted].

Burchard, H., Lange, X., Klingbeil, K., MacCready, P., 2019. Mixing estimates for estuaries. Journal of Physical Oceanography 49 (2), 631–648.

Burchard, H., Rennau, H., 2008. Comparative quantification of physically and numerically induced mixing in ocean models. Ocean Modelling 20 (3), 293–311.

Cheng, Y., Canuto, V., Howard, A., 2002. An improved model for the turbulent PBL. J. Atmos. Sci. 59, 1550–1565.

Gräwe, U., Holtermann, P., Klingbeil, K., Burchard, H., 2015. Advantages of vertically adaptive coordinates in numerical models of stratified shelf seas. Ocean Model. 92, 56–68.

Hansen, D., Rattray, M., 1965. Gravitational Circulation in Straits and Estuaries. Technical report (University of Washington. Department of Oceanography). Sears Founda-

tion for Marine Research.

Hetland, R. D., Geyer, W. R., 2004. An idealized study of the structure of long, partially mixed estuaries. Journal of Physical Oceanography 34 (12), 2677–2691.

Klingbeil, K., Becherer, J., Schulz, E., de Swart, H. E., Schuttelaars, H. M., Valle-Levinson, A., Burchard, H., 2019. Thickness-weighted averaging in tidal estuaries and the vertical distribution of the eulerian residual transport. Journal of Physical Oceanography 49 (7), 1809–1826.

Klingbeil, K., Mohammadi-Aragh, M., Gräwe, U., Burchard, H., 2014. Quantification of spurious dissipation and mixing–discrete variance decay in a finite-volume framework. Ocean Modelling 81, 49–64.

Knudsen, M., 1900. Ein hydrographischer Lehrsatz. Annalen der Hydrographie und Maritimen Meteorologie 28 (7), 316–320.

Lorenz, M., Klingbeil, K., MacCready, P., Burchard, H., 2019. Numerical issues of the total exchange flow (tef) analysis framework for quantifying estuarine circulation. Ocean Science 15 (3), 601–614.

MacCready, P., 2011. Calculating estuarine exchange flow using isohaline coordinates. Journal of Physical Oceanography 41 (6), 1116–1124.

MacCready, P., Geyer, W. R., 2010. Advances in estuarine physics. Annual Review of Marine Science 2, 35–58.

MacCready, P., Rockwell Geyer, W., Burchard, H., 2018. Estuarine Exchange Flow is Related to Mixing through the Salinity Variance Budget. J. Phys. Oceanogr. 48, 1375–1384.

McDougall, T. J., Barker, P. M., 2011. Getting started with teos-10 and the gibbs seawater (gsw) oceanographic toolbox. SCOR/IAPSO WG 127, 1–28.

Pietrzak, J., 1998. The use of TVD limiters for forward-in-time upstream-biased advection schemes in ocean modeling. Mon. Weather Rev. 126, 812–830.

Umlauf, L., Burchard, H., 2005. Second-order turbulence models for geophysical boundary layers. A review of recent work. Cont. Shelf Res. 25, 795–827.

Walin, G., 1977. A theoretical framework for the description of estuaries. Tellus 29, 128–136.

Walin, G., 1981. On the deep water flow into the Baltic. Geofysica 17, 75–93.

Waterson, N. P., Deconinck, H., 2007. Design principles for bounded higher-order convection schemes - a unified approach. J. Comput. Phys. 224, 182–207.

Selbstständigkeitserklärung

Ich versichere hiermit, dass ich die vorliegende Arbeit selbstständig verfasst und keine anderen als die angegebenen Quellen und Hilfsmittel benutzt habe. Ich versichere, dass die eingereichte elektronische Fassung mit den gedruckten Exemplaren übereinstimmt.

Rostock, 30.06.2020